4-2001

Dynamics of scalar dissipation in isotropic turbulence: a numerical and modelling study

Prakash Vedula
Georgia Institute of Technology - Main Campus

P. K. Yeung
Georgia Institute of Technology - Main Campus

Rodney O. Fox
Iowa State University, rofox@iastate.edu

Dynamics of scalar dissipation in isotropic turbulence: a numerical and modelling study

Abstract

The physical mechanisms underlying the dynamics of the dissipation of passive scalar fluctuations with a uniform mean gradient in stationary isotropic turbulence are studied using data from direct numerical simulations (DNS), at grid resolutions up to 512^3. The ensemble-averaged Taylor-scale Reynolds number is up to about 240 and the Schmidt number is from ⅛ to 1. Special attention is given to statistics conditioned upon the energy dissipation rate because of their important role in the Lagrangian spectral relaxation (LSR) model of turbulent mixing. In general, the dominant physical processes are those of nonlinear amplification by strain rate fluctuations, and destruction by molecular diffusivity. Scalar dissipation tends to form elongated structures in space, with only a limited overlap with zones of intense energy dissipation. Scalar gradient fluctuations are preferentially aligned with the direction of most compressive strain rate, especially in regions of high energy dissipation. Both the nature of this alignment and the timescale of the resulting scalar gradient amplification appear to be nearly universal in regard to Reynolds and Schmidt numbers. Most of the terms appearing in the budget equation for conditional scalar dissipation show neutral behaviour at low energy dissipation but increased magnitudes at high energy dissipation. Although homogeneity requires that transport terms have a zero unconditional average, conditional molecular transport is found to be significant, especially at lower Reynolds or Schmidt numbers within the simulation data range. The physical insights obtained from DNS are used for *a priori* testing and development of the LSR model. In particular, based on the DNS data, improved functional forms are introduced for several model coefficients which were previously taken as constants. Similar improvements including new closure schemes for specific terms are also achieved for the modelling of conditional scalar variance.

Disciplines

Aerospace Engineering | Chemical Engineering

Comments

This article is from *Journal of Fluid Mechanics*, 433 (2001): 29-60, doi: 10.1017/S0022112000003207. Posted with permission.

J. Fluid Mech. (2001), *vol.* 433, *pp.* 29–60. Printed in the United Kingdom

Dynamics of scalar dissipation in isotropic turbulence: a numerical and modelling study

By PRAKASH VEDULA[1], P. K. YEUNG[1] AND R. O. FOX[2]

[1]School of Aerospace Engineering, Georgia Institute of Technology, Atlanta, GA 30332, USA
e-mail: yeung@peach.ae.gatech.edu

[2]Department of Chemical Engineering, Iowa State University, Ames, IA 50011-2230, USA

(Received 20 April 2000 and in revised form 2 October 2000)

The physical mechanisms underlying the dynamics of the dissipation of passive scalar fluctuations with a uniform mean gradient in stationary isotropic turbulence are studied using data from direct numerical simulations (DNS), at grid resolutions up to 512^3. The ensemble-averaged Taylor-scale Reynolds number is up to about 240 and the Schmidt number is from $\frac{1}{8}$ to 1. Special attention is given to statistics conditioned upon the energy dissipation rate because of their important role in the Lagrangian spectral relaxation (LSR) model of turbulent mixing. In general, the dominant physical processes are those of nonlinear amplification by strain rate fluctuations, and destruction by molecular diffusivity. Scalar dissipation tends to form elongated structures in space, with only a limited overlap with zones of intense energy dissipation. Scalar gradient fluctuations are preferentially aligned with the direction of most compressive strain rate, especially in regions of high energy dissipation. Both the nature of this alignment and the timescale of the resulting scalar gradient amplification appear to be nearly universal in regard to Reynolds and Schmidt numbers. Most of the terms appearing in the budget equation for conditional scalar dissipation show neutral behaviour at low energy dissipation but increased magnitudes at high energy dissipation. Although homogeneity requires that transport terms have a zero unconditional average, conditional molecular transport is found to be significant, especially at lower Reynolds or Schmidt numbers within the simulation data range. The physical insights obtained from DNS are used for *a priori* testing and development of the LSR model. In particular, based on the DNS data, improved functional forms are introduced for several model coefficients which were previously taken as constants. Similar improvements including new closure schemes for specific terms are also achieved for the modelling of conditional scalar variance.

1. Introduction

It is well known that (Corrsin 1951; Batchelor 1959) efficient mixing in turbulence depends on a close coupling between advective transport which breaks large-scale non-uniformities of the scalar field into smaller scales, and molecular diffusion which tends to dissipate scalar fluctuations by acting on local gradients. The dissipation rate of a passive scalar fluctuation ϕ of diffusivity D_ϕ is defined here by

$$\chi = 2D_\phi \frac{\partial \phi}{\partial x_i} \frac{\partial \phi}{\partial x_i}, \tag{1}$$

where the factor of 2 is chosen such that the mean value $\langle\chi\rangle$ is the dissipation term in the equation for the scalar variance, $\langle\phi^2\rangle$. Being proportional to the square of scalar gradient fluctuations, the scalar dissipation rate is an important parameter of the small scales in the scalar field, which is known to be characterized by strong intermittency (Sreenivasan 1991; Warhaft 2000). The occurrence of large deviations from the mean is significant in, for example, turbulent combustion where extreme values of χ for the mixture fraction can cause local flame extinction.

A detailed understanding of the scalar dissipation is important, because of the physical significance noted above, and because of its direct role in the modelling of turbulent mixing, including probability density function (PDF) methods (Pope 1985; Dopazo 1994). In particular, the Lagrangian spectral relaxation (LSR) model proposed by Fox (1997, 1999) is a PDF model which attempts to incorporate the physics of scalar dissipation fluctuations. The LSR model is aimed at a full joint PDF description of the velocity, scalar, energy dissipation and scalar dissipation. By accounting for spectral transfer between different scales in the scalar field (Fox & Yeung 1999) it is able to avoid dubious assumptions of proportionality between the timescales of velocity and scalar fluctuations. Although the model is ultimately implemented in a Lagrangian frame following fluid particle trajectories, many of the assumptions used can, at least for homogeneous turbulence, be tested in an *a priori* manner in terms of Eulerian quantities.

Our objectives in this paper are to study the dynamics underlying the evolution of the scalar dissipation rate in relation to the local kinematics of the velocity field, and to use this information to achieve improvements in modelling. For simplicity, we consider the case of a homogeneous scalar fluctuation field subject to a uniform mean gradient ($\nabla\Phi$) in isotropic turbulence. The instantaneous scalar dissipation equation can be written as

$$\begin{aligned}\frac{\mathrm{D}\chi}{\mathrm{D}t} &\equiv \frac{\partial\chi}{\partial t} + u_i\frac{\partial\chi}{\partial x_i} \\ &= D_\phi\frac{\partial^2\chi}{\partial x_i\partial x_i} - 4D_\phi\frac{\partial\phi}{\partial x_j}\frac{\partial u_i}{\partial x_j}\frac{\partial\Phi}{\partial x_i} - 4D_\phi\frac{\partial\phi}{\partial x_i}\frac{\partial\phi}{\partial x_j}s_{ij} - 4D_\phi^2\left(\frac{\partial^2\phi}{\partial x_i\partial x_j}\right)^2, \qquad (2)\end{aligned}$$

where $\mathrm{D}/\mathrm{D}t$ denotes the material derivative, and the four terms on the right-hand side represent, respectively: (i) transport by molecular diffusion, (ii) production by the mean scalar gradient, (iii) nonlinear amplification or 'stretching' by strain rate fluctuations (s_{ij}), and (iv) destruction of dissipation fluctuations by molecular diffusivity. It may be noted that the transport terms have zero space averages because of homogeneity. The mean gradient term is expected to be small, if the fluctuating gradients are much larger than the mean gradient and if the scalar field does not deviate dramatically from local isotropy. For these reasons, the general expectation, to be checked in this work, is that the nonlinear amplification and molecular destruction are the dominant terms, especially at high Reynolds number.

In equation (2) the nonlinear amplification term is of special interest because it contains the coupling between the velocity and scalar fields whereby scalar gradients are amplified by association with the local straining of fluid elements. The magnitude, as well as the sign, of this term depends on the geometric alignment between scalar gradients and strain rates, which, because of the tensorial structure involved, is best studied in the coordinate frame defined by the principal axes of the strain-rate tensor. In this coordinate frame the strain-rate tensor is represented by its diagonal elements, which we arrange in the order $\alpha \geqslant \beta \geqslant \gamma$, with (given the incompressibility condition

$\alpha + \beta + \gamma = 0$) $\alpha > 0$ being the most extensive and $\gamma < 0$ being the most compressive. Although the statistics of principal strain rates have been studied numerically by other authors (e.g. Ashurst *et al.* 1987; Yeung, Girimaji & Pope 1990), more comprehensive information is needed in this work, particularly concerning conditional statistics of scalar gradient alignment and the possible dependence of these quantities on Reynolds number and Schmidt number. Issues of vector alignment with principal strain directions are also important in other contexts (e.g. Boratav, Elghobashi & Zhong 1998; Nomura & Post 1998).

In this paper, we make use of data from direct numerical simulations (DNS), which allow us to investigate physical processes in great detail (see Moin & Mahesh 1998 for a review). For example, subject to some numerical and statistical limitations, we can calculate each term in (2) as well as scalar gradients projected along the principal strain directions. Considerable emphasis is placed on extracting quantities relevant to the LSR model (Fox 1997, 1999), especially concerning the dynamics of the scalar dissipation rate conditioned on energy dissipation fluctuations (ϵ) representing the instantaneous rate of strain in the flow. DNS results are also used to develop improved functional forms of the model expressions, in several cases suggesting the replacement of constant coefficients with more general formulations as functions of the conditioning variable. Currently, we consider only single-scalar statistics at ensemble-averaged Taylor-scale Reynolds numbers (R_λ) from 38 to 243 and at Schmidt numbers ($Sc \equiv \nu/D_\phi$) from $\frac{1}{8}$ to 1. Extension of this work to the important topic of differential diffusion (Bilger & Dibble 1982; Fox 1999) of multiple scalars with different molecular diffusivities is the subject of a future paper.

The rest of this paper is organized as follows. In § 2, we give a brief account of the LSR model formulation and identify the specific motivation behind the need for a number of quantities from DNS. In § 3, we provide a brief overview of the numerical simulation approach and the methods used for data analysis including statistical sampling issues for conditional expectations. DNS results aimed at physical understanding are given in § 4, including statistics of principal strain rates, alignment of scalar gradients, and conditional averages of the dissipation, variance and Laplacian of the scalar field. It should be noted that the conditional averages studied in this paper are different from those conditioned on the scalar fluctuation (e.g. Jaberi, Miller & Givi 1996; Overholt & Pope 1996; Yeung 1998). Issues concerning model development are addressed in § 5, in part via the 'budget' of terms contributing to the conditional rates of change of the scalar variance and its dissipation rate. Some numerical details on the new model coefficients are collected into an Appendix. A summary of the main results and conclusions is provided in § 6.

2. Background on model formulation

The spectral relaxation (SR) model was initially proposed by Fox (1995) to describe non-equilibrium scalar spectral effects on the scalar dissipation rate. In the SR model, the scalar variance spectrum is divided into discrete wavenumber bands (denoted by $\langle \phi^2 \rangle_i$, with i here being a band index starting from unity), each with its own characteristic timescale that can be related to the scalar transfer spectrum (Fox & Yeung 1999). The final wavenumber band in the scalar cascade corresponds to the scalar dissipation range: $\kappa \in [\kappa_D, \infty)$ where $\kappa_D = C_D^{1/2} Sc^{1/2} \kappa_\eta$, $C_D \approx 0.01$ is a model constant, and $\kappa_\eta = (\langle \epsilon \rangle / \nu^3)^{1/4}$ is the Kolmogorov-scale wavenumber. For statistically stationary, homogeneous scalar mixing (the configuration studied in this paper), the scalar spectrum reaches a dynamic equilibrium wherein the scalar-variance production

due to the mean scalar gradient is in balance with the scalar dissipation rate. In this limit, the SR model can be simplified since all wavenumber bands are in dynamic equilibrium. The spectral scalar flux into the scalar dissipation range (which depends explicitly on the scalar spectral content in the neighbouring wavenumber band) can be approximated by the mean scalar dissipation rate $\langle\chi\rangle$. The model equation for the scalar dissipation rate can then be uncoupled from the equations describing the scalar spectral cascade (i.e. the equations for the $\langle\phi^2\rangle_i$). In this work, we shall compare the model equations to DNS results only in this limiting case.

The SR model was extended by Fox (1997, 1999) to include the effects of Lagrangian fluctuations of the scalar dissipation rate on the turbulent mixing of scalars subject to molecular diffusion. In the LSR model, Lagrangian fluctuations in the scalar dissipation rate are expressed via the conditional expected value $\langle\chi|\epsilon = \epsilon^*\rangle$, hereinafter referred to as the conditional scalar dissipation rate. In Lagrangian PDF models (Pope 1994), the superscript * is often used to denote the value of a quantity following a fluid particle through the flow. In the LSR model, $\langle X\rangle^*$ is used to denote the Lagrangian expected value of X conditioned on ϵ^*. The Lagrangian PDF models for such quantities are related to Eulerian conditional statistics by (Pope 1994)

$$\frac{\mathrm{d}\langle X\rangle^*}{\mathrm{d}t} = \left\langle \frac{\mathrm{D}X}{\mathrm{D}t}\middle| \epsilon = \epsilon^* \right\rangle, \tag{3}$$

where the right-hand side is the Eulerian conditional expected value of the material derivative of $X(\boldsymbol{x}, t)$ evaluated at $\epsilon(\boldsymbol{x}, t) = \epsilon^*(t)$. This equation is, in fact, the definition of $\langle X\rangle^*$. The task of modelling here is to try to express the right-hand side in terms of known quantities, as is done in this paper for the limiting case of statistically stationary, homogeneous scalar mixing. (An *a posteriori* test of equation (3) requires comparisons of Lagrangian statistics between DNS and model, which are in progress and will be reported in future communications.) As described above, we will again represent the flux of conditional scalar fluctuations into the scalar dissipation range by $\langle\chi\rangle^*$, so that the LSR model equation for the conditional scalar dissipation rate can be decoupled from the equations for contributions to the conditional scalar variance in different wavenumber bands (i.e. $\langle\phi^2\rangle_i^*$).

For statistically stationary, homogeneous turbulent scalar mixing, the Eulerian conditional statistics required to close the right-hand side of equations in the form of (3) can be extracted directly from DNS for comparison with the LSR model. Note, however, that because conditional averaging and differentiation, in general, do not commute with each other (Klimenko & Bilger 1999), statistical stationarity does not imply that the right-hand side of (3) is null. In addition, in (3), $\epsilon^*(t)$ is a (statistically stationary) random process which will generate time-dependent fluctuations in $\langle X\rangle^*$. Nevertheless, unlike 'standard' Lagrangian PDF models (Pope 1994) which introduce a 'white-noise' driving force, all random processes in the LSR model will be deterministic in the limit where $\epsilon^*(t) = \langle\epsilon\rangle$ (i.e. when $\epsilon^*(t)$ is constant). In this sense, intermittency in the scalar mixing process is directly linked to intermittency in the turbulent dissipation rate as described by the stochastic model for $\epsilon^*(t)$ (Fox 1997). Finally, it is important to note that the statistics of $\chi^*(t)$ (the instantaneous scalar dissipation rate) and $\langle\chi\rangle^*(t)$ will be very different (although they share the same unconditional mean). Indeed, as can be seen from figure 11 in Fox (1997), $\langle\chi\rangle^*(t)$ is a relatively smooth random process whereas $\chi^*(t)$ is (see figure 1 in Yeung 2001) highly intermittent. This difference has important consequences when modelling the molecular mixing rate of the scalar field $\phi^*(t)$. In particular, when $\langle\chi\rangle^*(t)$ is used in the molecular-mixing closure, the scalar field exhibits a very modest tendency towards

non-Gaussian behaviour (Fox 1997), but is otherwise well behaved. On the other hand, when $\chi^*(t)$ is used, the resulting model yields a very poor representation of the scalar PDF (Pope 1999, personal communication).

In the LSR model, conditional statistics of the type appearing in the right-hand side of (3) are modelled using conditional moments involving the scalar and its dissipation rate. For example, in the limit of a fully developed scalar spectrum, the evolution of conditional scalar variance $\langle\phi^2\rangle^*$ is modelled by (Fox 1997)

$$\left\langle \frac{\mathrm{D}\phi^2}{\mathrm{D}t} \middle| \epsilon = \epsilon^* \right\rangle_{LSR} = -2\langle u_i\phi\rangle \frac{\partial \Phi}{\partial x_i} + f_D \frac{\langle\chi\rangle}{\langle\phi^2\rangle} \left(\langle\phi^2\rangle - \langle\phi^2\rangle^*\right) - \langle\chi\rangle^*, \tag{4}$$

where f_D is a model constant of order one. This model can be compared to the exact Eulerian expression:

$$\left\langle \frac{\mathrm{D}\phi^2}{\mathrm{D}t} \middle| \epsilon \right\rangle_{exact} = -2\langle u_i\phi|\epsilon\rangle \frac{\partial \Phi}{\partial x_i} + \left\langle D_\phi \frac{\partial^2\phi^2}{\partial x_i \partial x_i} \middle| \epsilon \right\rangle - \langle\chi|\epsilon\rangle, \tag{5}$$

where it can be seen that two modelling assumptions have been introduced:

$$\langle u_i\phi|\epsilon\rangle = \langle u_i\phi\rangle \tag{6}$$

$$\left\langle D_\phi \frac{\partial^2\phi^2}{\partial x_i \partial x_i} \middle| \epsilon \right\rangle = f_D \frac{\langle\chi\rangle}{\langle\phi^2\rangle} \left(\langle\phi^2\rangle - \langle\phi^2|\epsilon\rangle\right). \tag{7}$$

(For inhomogeneous scalar mixing, an additional term $D_\phi \nabla^2\langle\phi^2|\epsilon\rangle$ would also appear on the right-hand side of equation (7). However, terms of this form are null in homogeneous flows and thus have not been included in this work.) In § 5, we find from the DNS data that these modelling assumptions can be significantly improved, and thus new closures are developed in favour of (4).

In order to form a closed system, an equation for the conditional scalar dissipation rate must be coupled to (4) above. For a statistically stationary flow, the LSR model expression has the form

$$\left\langle \frac{\mathrm{D}\chi}{\mathrm{D}t} \middle| \epsilon = \epsilon^* \right\rangle_{LSR} = -\gamma_D \frac{\langle\chi\rangle^*}{\langle\phi^2\rangle_D^*} \langle u_i\phi\rangle \frac{\partial \Phi}{\partial x_i} + C_B \left(\frac{\epsilon^*}{\nu}\right)^{1/2} \langle\chi\rangle^* - C_d \frac{\langle\chi\rangle^*}{\langle\phi^2\rangle_D^*} \langle\chi\rangle^*, \tag{8}$$

where γ_D, C_B and C_d are model coefficients to be discussed further, and the subscript D on the term $\langle\phi^2\rangle_D^*$ signifies contributions from the wavenumber range $\kappa > \kappa_D$ only. Comparison of (8) with equation (38) in Fox (1999) (in which the scalar dissipation was denoted by ϵ_ϕ and without a factor of 2, such that $\langle\epsilon_\phi\rangle^* = \frac{1}{2}\langle\chi\rangle^*$) shows two significant differences. First, owing to statistical stationarity, the terms containing C_D and C_s in the older model are now combined to form the term containing C_B in (8) (see Appendix in Fox 1999). Secondly, as discussed below, the two molecular dissipation terms in equation (38) of Fox (1999) have been combined in (8).

Some understanding of the relative importance of different terms on the right-hand side of (8) can be obtained by considering the timescales involved. In particular, the characteristic timescale associated with both mean gradient and molecular dissipation (first and third) terms is given by $\tau_D = \langle\phi^2\rangle_D^*/\langle\chi\rangle^*$ where the scalar variance is taken only from the dissipation range $\kappa > \kappa_D$. The corresponding Eulerian term for $\langle\phi^2\rangle_D^*$, i.e. $\langle\phi^2|\epsilon\rangle_D$, is computed from the scalar field after a filtering operation that – in contrast to the usual practice in large-eddy simulations – involves removing all spectral content below the cutoff wavenumber κ_D. As confirmed in an earlier study (Fox & Yeung 1999), for a statistically stationary flow, high-Reynolds-number

scaling in the range $Sc \gtrsim 1$ requires that this quantity be inversely proportional to the Taylor-scale Reynolds number R_λ: i.e. $\langle \phi^2|\epsilon\rangle_D \sim \langle \phi^2|\epsilon\rangle / R_\lambda$. By assuming that the ratio between the large-eddy timescales of the velocity (as $K/\langle\epsilon\rangle$, where K is the kinetic energy) and scalar fields (as $\langle\phi^2\rangle/\langle\chi\rangle$) approaches a constant at high Reynolds number we can obtain an order-of-magnitude estimate

$$\frac{\langle \phi^2|\epsilon\rangle_D}{\langle \chi|\epsilon\rangle} \sim \frac{K}{\langle\epsilon\rangle}\frac{1}{R_\lambda}, \tag{9}$$

which furthermore can be recognized as being proportional to the Kolmogorov timescale, $\tau_\eta = (\nu/\langle\epsilon\rangle)^{1/2}$. In other words, both nonlinear amplification (second term) and molecular dissipation (third term) in (8) vary on the same timescale, so that they are both dynamically important. On the other hand, although (subject to a Reynolds-number dependence for the coefficient γ_D) the mean gradient term also has the same timescale, because the unconditional scalar flux is used in (8), it is expected that at high values of the energy dissipation it would be small when compared to other terms in the same equation.

The exact Eulerian expression for the right-hand side of the Lagrangian PDF model for $\langle\chi\rangle^*$ follows from (2):

$$\left\langle \frac{\mathrm{D}\chi}{\mathrm{D}t}\middle|\epsilon\right\rangle_{exact} = \left\langle D_\phi \frac{\partial^2\chi}{\partial x_i \partial x_i}\middle|\epsilon\right\rangle - 4\left\langle D_\phi \frac{\partial u_i}{\partial x_j}\frac{\partial\phi}{\partial x_j}\middle|\epsilon\right\rangle \frac{\partial \Phi}{\partial x_i} - 4\left\langle D_\phi \frac{\partial\phi}{\partial x_i} s_{ij} \frac{\partial\phi}{\partial x_j}\middle|\epsilon\right\rangle - 4\left\langle \left(D_\phi \frac{\partial^2\phi}{\partial x_i \partial x_j}\right)^2\middle|\epsilon\right\rangle. \tag{10}$$

Comparing with (8), it can be seen that the following three modelling assumptions have been introduced:

$$-4\left\langle D_\phi \frac{\partial\phi}{\partial x_i} s_{ij} \frac{\partial\phi}{\partial x_j}\middle|\epsilon\right\rangle = C_B \left(\frac{\epsilon}{\nu}\right)^{1/2} \langle\chi|\epsilon\rangle, \tag{11}$$

$$4\left\langle D_\phi \frac{\partial u_i}{\partial x_j}\frac{\partial\phi}{\partial x_j}\middle|\epsilon\right\rangle = \gamma_D \frac{\langle\chi|\epsilon\rangle}{\langle\phi^2|\epsilon\rangle_D}\langle u_i\phi\rangle_D, \tag{12}$$

$$4\left\langle \left(D_\phi \frac{\partial^2\phi}{\partial x_i\partial x_j}\right)^2\middle|\epsilon\right\rangle - \left\langle D_\phi \frac{\partial^2\chi}{\partial x_i\partial x_i}\middle|\epsilon\right\rangle = C_d \frac{\langle\chi|\epsilon\rangle}{\langle\phi^2|\epsilon\rangle_D}\langle\chi|\epsilon\rangle. \tag{13}$$

Note that in earlier versions of the model (e.g. equation (38) in Fox 1999), in analogy with (7), the second term on the left-hand side of (13) was modelled separately, as

$$\left\langle D_\phi \frac{\partial^2\chi}{\partial x_i\partial x_i}\middle|\epsilon\right\rangle = \gamma_d \frac{\langle\chi\rangle}{\langle\phi^2\rangle_D}\left(\langle\chi\rangle - \langle\chi|\epsilon\rangle\right), \tag{14}$$

and was assumed to be much smaller than the first at high Reynolds numbers. However, at low Reynolds numbers, the DNS data reveal that both terms on the left of (13) are of nearly equal magnitude for large ϵ, and that C_d varies significantly with Reynolds number when a separate model is used for the second term. Thus, based on the results of the present study, these two terms have been combined in the current version of the model. As will be shown in § 5, this regrouping yields improved agreement with the DNS data using a single value of C_d over the entire range of Reynolds numbers investigated.

In deriving the LSR model (Fox 1997, 1999), the model constants γ_D, C_B, and

C_d were previously assigned the same values as were employed in the SR model for the unconditional scalar dissipation rate (Fox 1995). For example, $C_B = 0.5$ corresponds to Batchelor's constant (Batchelor 1959). For C_d, the extreme values of 3 and $\frac{5}{3}$ correspond, respectively, to the limiting cases of random scalar fields dominated by one-dimensional diffusive layers and those without local structure in three-dimensional space. (The self-similar decay of such random scalar fields by molecular diffusion alone in the absence of turbulence was studied in Fox 1994; a fully developed turbulent flow is expected to generate a scalar field between these limits.) For statistically stationary, homogeneous scalar mixing, all terms in (11)–(13) can be computed from DNS data, and thus the modelling assumptions can be tested directly. In an earlier work (Fox & Yeung 1999), it was found that the values of the model constants are quite sensitive to the choice of the cutoff wavenumber κ_D. However, κ_D can be chosen independently by specifying that the filtered scalar field must contain a fixed and large fraction of the dissipation rate of the unfiltered scalar field. In this work, the choice $\kappa_D = 0.1Sc^{1/2}\kappa_\eta$ was found to capture over 90% of the unfiltered scalar dissipation rate, and to yield values for C_d close to 3 over a wide range of Reynolds and Schmidt numbers.

In addition to uncertainties in the values of the model constants, it should be noted that the functional forms of the terms in the LSR model were also chosen based on scaling arguments for unconditional statistics (Fox 1997, 1999). Thus, one of the goals of this work is to compare equations (6), (7) and (11)–(13) with the DNS data (i.e. *a priori* model validation), and to suggest new functional forms when the agreement is poor. (We have already introduced one such model improvement in arriving at (13).) For example, in § 5, we find that agreement between model and DNS can be significantly improved by simply letting the 'constants' (i.e. f_D, γ_D, C_B and C_d) become functions of the conditioning variable ϵ. Moreover, by using DNS data over a range of Reynolds and Schmidt numbers, we are able to demonstrate that the resulting functional forms are nearly independent of these parameters.

3. Numerical simulation overview

We analyse velocity and scalar field data obtained from direct numerical simulations carried out using a parallelized version of the algorithm of Rogallo (1981), which is Fourier pseudo-spectral in space and second-order in time. As in Yeung (1998), the velocity field considered is stationary isotropic turbulence with energy maintained by forcing at the large scales (Eswaran & Pope 1988). As a result of an approximate balance between production by mean scalar gradient and molecular dissipation, the scalar fluctuations are also statistically stationary in time. This stationarity allows data at well-separated time intervals (of order one large-eddy turnover time or more) in DNS to be taken as independent realizations for ensemble averaging. Both the simulation and data analysis were carried out on an IBM SP, using up to 64 processors for calculations with 512^3 grid points.

A common goal in DNS is to reach the highest Reynolds number possible while maintaining accuracy at the small scales. In our work, the Reynolds number reached ($R_\lambda \approx 243$) is sufficiently high for a limited inertial range in the energy spectrum to occur, with a value of the Kolmogorov spectrum constant (Yeung & Zhou 1997) in good agreement with experiments (Sreenivasan 1995). Resolution of the small scales is measured by the non-dimensional parameter $k_{max}\eta$, where $k_{max} = \sqrt{2}N/3$ is (allowing for alias error control) the highest wavenumber resolved on an N^3 grid, and η is the Kolmogorov lengthscale. For most purposes (e.g. in Ruetsch & Maxey 1991;

Grid	256^3	256^3	256^3	512^3
R_λ	38	90	141	243
$k_{max}\eta$	5.82	3.04	1.41	1.40
Sc	$\frac{1}{4}$, 1	$\frac{1}{8}$, $\frac{1}{4}$, 1	$\frac{1}{8}$, 1	$\frac{1}{8}$, 1
M	14	11	10	23

TABLE 1. Basic parameters of the numerical simulations. Ensemble averages are taken over M realizations at each grid resolution.

Pumir 1994; Overholt & Pope 1996; Yeung 1998) $k_{max}\eta \approx 1.5$ is usually considered sufficient for passive scalars of Schmidt numbers of 1.0 or less. However, it should be emphasized that, at given R_λ and Sc, resolution requirements depend on the nature of the quantity computed. In particular, whereas $k_{max}\eta \approx 1.5$ is sufficient for quantities which are second order or lower in scalar gradients (including dissipation rate and alignment properties studied in § 4.1), we find that a higher level of resolution is required for higher-order quantities, such as derivatives of the scalar dissipation rate arising in its transport equation (equation (2)). To meet this requirement, we have used, subject to practical constraints on computational time, relatively refined grids, even for simulations at low Reynolds number. It may be noted that this strategy is similar to that used (Bogucki, Domaradzki & Yeung 1997; Brethouwer & Nieuwstadt 1999; Yeung, Sykes & Vedula 2000) to perform DNS for scalars with $Sc > 1$ which are characterized by fluctuations arising at scales smaller than those of the velocity field.

A summary of the actual simulation parameters is given in table 1, including the number of grid points, Reynolds number, the parameter $k_{max}\eta$, Schmidt numbers, and the number of realizations (M) used for ensemble averaging in each case. The highest degree of resolution used is $k_{max}\eta \approx 6$, for the case of lowest Reynolds number (at R_λ 38). Because of the resolution issues discussed above, results for the $Sc = 1.0$ scalar at the two highest Reynolds numbers (with $k_{max}\eta \approx 1.5$) in this work should be taken with caution.

Given its prominent role in the LSR model equations (§ 2), a detailed understanding of the behaviour of energy dissipation fluctuations is important. A qualitative view of the spatial structure is given in figure 1 which shows contours in a two-dimensional plane (for a single realization) for the normalized fluctuation $\epsilon/\langle\epsilon\rangle$ at the lowest and highest Reynolds numbers in this work. It can be seen that regions of high ϵ (relative to the mean) are confined in localized regions of space. This implies that samples of large $\epsilon/\langle\epsilon\rangle$ are relatively rare in the solution domain, which is consistent with the expected behaviour for intermittent quantities. It should be noted that the appearance of contour plots depends somewhat on the choice of contour levels (see figure captions). Nevertheless, between figures 1(a) and 1(b) the expected increase in intermittency at higher Reynolds number is clearly illustrated by a reduction in the thickness of the narrow zones of intense dissipation. This observation is also accompanied by higher peak normalized contour levels. (It is also seen that contour lines in figure 1(a) are remarkably smooth, which, however, is not a true Reynolds number effect but is instead mainly due to the higher level of resolution ($k_{max}\eta \approx 6$) used for the R_λ 38 data.)

Figure 2 shows similar contours for the normalized scalar dissipation rate ($\chi/\langle\chi\rangle$), for scalars of $Sc = \frac{1}{8}$ and 1, respectively, in the 512^3 data at R_λ 243. Localized

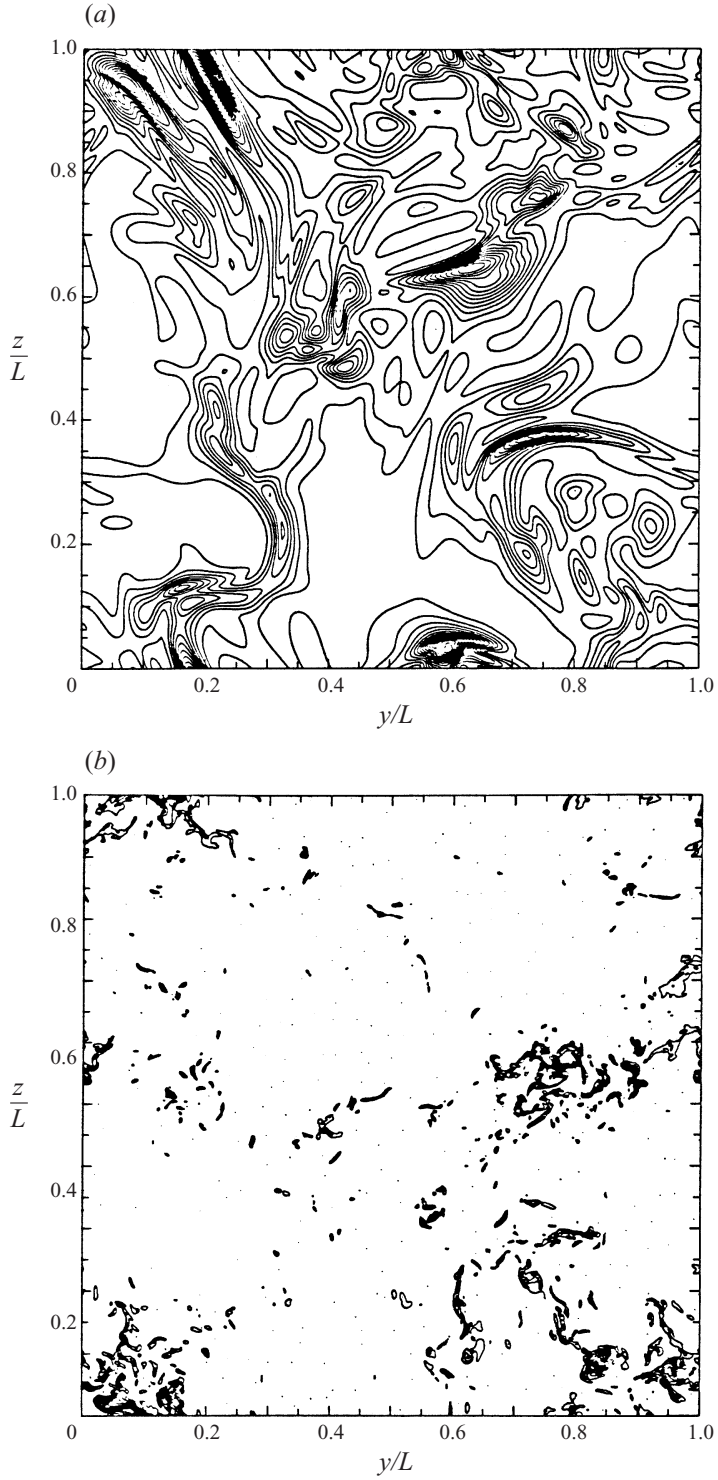

FIGURE 1. (*a*) Sample contour plot of normalized instantaneous energy dissipation rate ($\epsilon/\langle\epsilon\rangle$) at R_λ 38 for a chosen two-dimensional plane. Contour levels are from 0.5 to 10 in increments of 0.5. The coordinates in the plane (y, z) are normalized by the length of the solution domain (L). (*b*) Same as (*a*), but for R_λ 243, with contour levels from 2 to 42 by increments of 2.0.

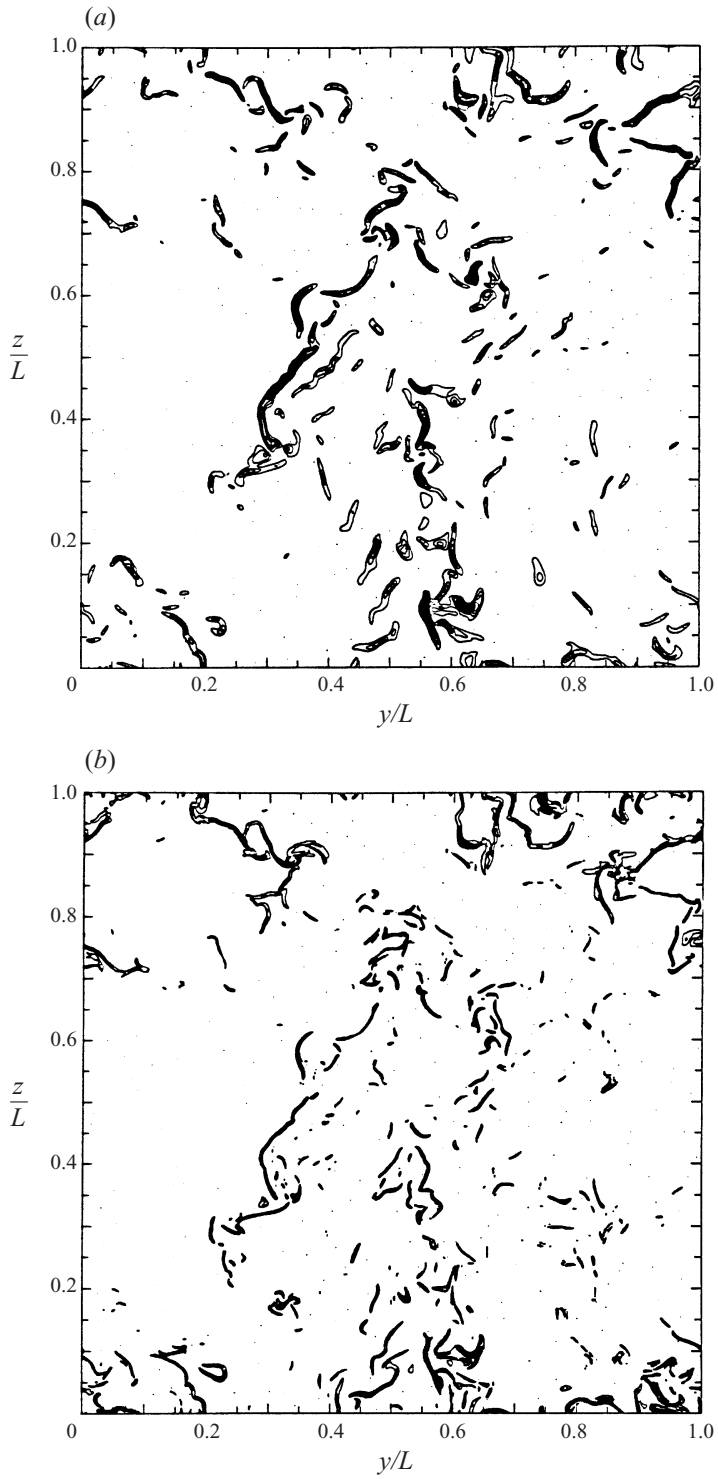

FIGURE 2. (*a*) Same as figure 1(*b*), but for normalized scalar dissipation ($\chi/\langle\chi\rangle$) for scalar of $Sc = \frac{1}{8}$. Contour levels are from 2.5 to 50 by increments of 2.5. (*b*) Same as (*a*), but scalar of $Sc = 1.0$. Contour levels are from 2.5 to 57.5 by increments of 2.5.

Grid	256^3	256^3	256^3	512^3
R_λ	38	90	141	243
$\sigma(\epsilon)/\mu(\epsilon)$	0.97	1.15	1.24	1.46
$\mu_3(\epsilon)$	2.86	4.08	4.49	6.31
$\mu_4(\epsilon)$	19	37	44	114
$\sigma^2(\ln\epsilon)$	0.81	0.97	1.07	1.25
$\mu_3(\ln\epsilon)$	−0.25	−0.18	−0.15	−0.09
$\mu_4(\ln\epsilon)$	3.23	3.16	3.09	3.07
$\{\epsilon/\langle\epsilon\rangle\}_{Z=-1}$	0.28	0.23	0.21	0.18
$\{\epsilon/\langle\epsilon\rangle\}_{Z=0}$	0.68	0.62	0.60	0.54
$\{\epsilon/\langle\epsilon\rangle\}_{Z=1}$	1.68	1.66	1.69	1.64
$\{\epsilon/\langle\epsilon\rangle\}_{Z=2}$	4.14	4.45	4.73	5.01
$\{\epsilon/\langle\epsilon\rangle\}_{Z=3}$	10.17	11.91	13.32	15.29
$\{\epsilon/\langle\epsilon\rangle\}_{Z=4}$	25.02	31.90	37.54	46.67
$\{\epsilon/\langle\epsilon\rangle\}_{Z=5}$	61.55	85.41	105.77	142.46

TABLE 2. Statistical measures of the energy dissipation rate. The symbols $\mu(\cdot)$, $\sigma(\cdot)$, $\sigma^2(\cdot)$, $\mu_3(\cdot)$ and $\mu_4(\cdot)$ denote the mean, r.m.s., variance, skewness and flatness (respectively) of the bracketed quantities.

Grid	256^3	256^3	256^3	256^3	256^3	256^3	256^3	512^3	512^3
R_λ	38	38	90	90	90	141	141	243	243
Sc	$\frac{1}{4}$	1	$\frac{1}{8}$	$\frac{1}{4}$	1	$\frac{1}{8}$	1	$\frac{1}{8}$	1
$\langle\phi^2\rangle$	1.18	2.03	2.44	2.88	3.74	1.70	2.27	2.63	3.07
$\langle\chi\rangle$	2.31	2.65	2.31	2.38	2.38	2.01	2.06	2.69	2.70
r_ϕ	2.66	1.77	3.17	2.76	2.13	3.14	2.41	2.87	2.48
$\sigma(\chi)/\mu(\chi)$	4.60	9.52	6.89	9.81	14.05	8.38	12.05	21.68	25.36
$\mu_3(\chi)$	4.85	6.28	5.39	6.32	7.76	6.64	7.56	9.90	10.41
$\mu_4(\chi)$	42	72	52	73	112	78	103	182	241
$\sigma^2(\ln\chi)$	1.86	2.59	2.13	2.51	3.22	2.60	3.31	3.37	3.73
$\mu_3(\ln\chi)$	−0.174	−0.115	−0.113	−0.056	−0.098	−0.065	−0.055	−0.018	−0.012
$\mu_4(\ln\chi)$	3.13	2.87	3.05	2.90	2.82	2.88	2.81	2.82	2.82

TABLE 3. Statistical moments involving the scalar dissipation rate.

packets of intense 'activity' which characterize intermittency are again observed. However, compared to energy dissipation in the same simulation (figure 1*b*), the scalar dissipation has a more defined structure, with intense values concentrated in narrow but elongated bands, especially at higher Schmidt number. This elongated structure is consistent with the picture suggested by previous studies (Sreenivasan 1991). In addition, it suggests that intense scalar gradients tend to reside in sheets, a feature also implied in experimental measurements at relatively high resolution (Buch & Dahm 1996, 1998; Mydlarski & Warhaft 1998*a*; Mydlarski *et al.* 1998).

In figures 1(*b*), 2(*a*) and 2(*b*) regions of high ϵ and high χ appear to have only a limited degree of overlap. The overlap between χ at different Schmidt numbers is much stronger, which is consistent with a significant cross-correlation between the gradients of different scalars (Yeung 1998). Reference to the normalized contour levels indicates that, consistent with other observations in both simulations (Overholt & Pope 1996; Wang, Chen & Brasseur 1999; Yeung 2001) and experiments (Warhaft 2000), the scalar field at the small scales is much more intermittent than the velocity field, especially at higher Schmidt number.

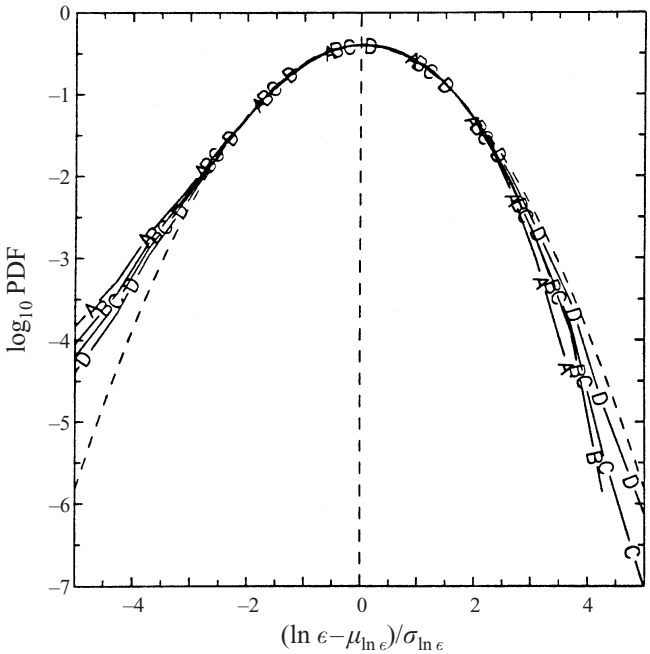

FIGURE 3. Standardized PDFs of $\ln \epsilon$ from data at R_λ 38, 90, 141 and 243 denoted by lines A to D, respectively (with the grid resolutions given in table 1). Dashed curve represents a Gaussian distribution.

To provide more information on the statistical properties of ϵ and χ we show a number of statistical moments in tables 2 and 3, as well as PDFs of their logarithms, respectively, in figures 3 and 4. The skewness and flatness of both ϵ and χ, as well as the variances of their logarithms, provide quantitative indications of increase in intermittency with both Reynolds number and Schmidt number. Despite well-known reservations concerning log-normal distributions in turbulence (Frisch 1995; Wang *et al.* 1996), it can be seen in figure 3 that (within the range of our DNS data) the PDF of $\ln \epsilon$ does become closer to Gaussian with increase in Reynolds number. This observation, which is important for our sampling purposes, is also supported by the fact that (see table 2) the skewness and flatness factors of $\ln \epsilon$ become closer to the values 0 and 3, respectively, at higher Reynolds number.

The Reynolds and Schmidt number combinations in figure 4 are chosen so that inferences about the effects of both parameters can be made in a single plot. However, unlike $\ln \epsilon$, $\ln \chi$ displays no clear trend of increasing Gaussianity at higher Reynolds number, with a flatness factor (see table 3) which is slightly below the Gaussian value of 3. (In experimental data by Jayesh & Warhaft (1992) and Buch & Dahm (1998) at $Sc \approx 1$, the PDF of $\ln \chi$ is close to Gaussian with a slight negative skewness.) However, comparison between tables 2 and 3 shows that the skewness and flatness factors of the scalar dissipation are, even for $Sc = \frac{1}{8}$, greater than those of the energy dissipation. These observations provide additional support, at least in our DNS data range, that scalar fluctuations are more intermittent than the velocity.

Within the limits of statistical uncertainty (in, say, skewness and flatness factors of χ in table 3), the current results can be interpreted as suggesting a definite increase in intermittency with Reynolds number at fixed Schmidt number. This Reynolds number trend is different from numerical simulations of two-dimensional Gaussian

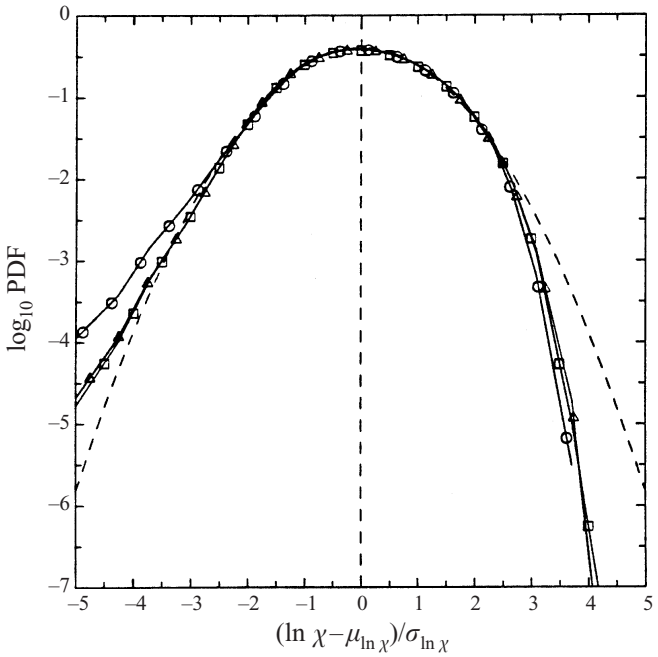

FIGURE 4. Standardized PDFs of $\ln \chi$ for ○, R_λ 90, $Sc = \frac{1}{8}$; △, R_λ 243, $Sc = \frac{1}{8}$; □, R_λ 243, $Sc = 1$.

random fields (Holzer & Siggia 1994; Chen & Kraichnan 1998) which indicate strong intermittency for scalar fields even at very low Reynolds number and in the absence of intermittency in the velocity field itself. This contrast may be due to intrinsic differences between the nature of the velocity fields studied in this work versus those which are kept Gaussian at all times and do not evolve according to the dynamics of the Navier–Stokes equations.

As indicated in § 2, for the purpose of model development, accurate results for the conditional expectations of various variables given the energy dissipation are required. Difficulties in data ranges where relatively few conditional samples exist (usually at the tails of its PDF) are well-known (e.g. Fox 1996; Yeung 1998). Whereas greater sampling accuracy can, in principle, be achieved by taking more realizations in DNS, in practice, we are limited by the amount of computational resources available. Use of an intermittent quantity such as the dissipation rate as conditioning variable increases these difficulties, because the sampling range of interest would then extend far from the mean, while the number of samples falling into outlying intervals may not be sufficient to produce a statistically reliable conditional average.

The difficulty above is partially alleviated by using the logarithm ($\ln \epsilon$) of the energy dissipation as the conditioning variable instead, the main advantage being that (as suggested by skewness and flatness factors in table 2) $\ln \epsilon$ is approximately Gaussian in the simulations, especially at high Reynolds numbers. Since a one-to-one relationship exists between ϵ and $\ln \epsilon$, a plot of conditional averages given $\ln \epsilon$ on a linear scale can be interpreted as the same quantities given ϵ but with ϵ on logarithmic scales. In particular, for the conditional average of a quantity Q we can write

$$\langle Q | \epsilon = \epsilon' \rangle = \left\langle Q \mid Z = \frac{\ln \epsilon' - \mu_{\ln \epsilon}}{\sigma_{\ln \epsilon}} \right\rangle, \tag{15}$$

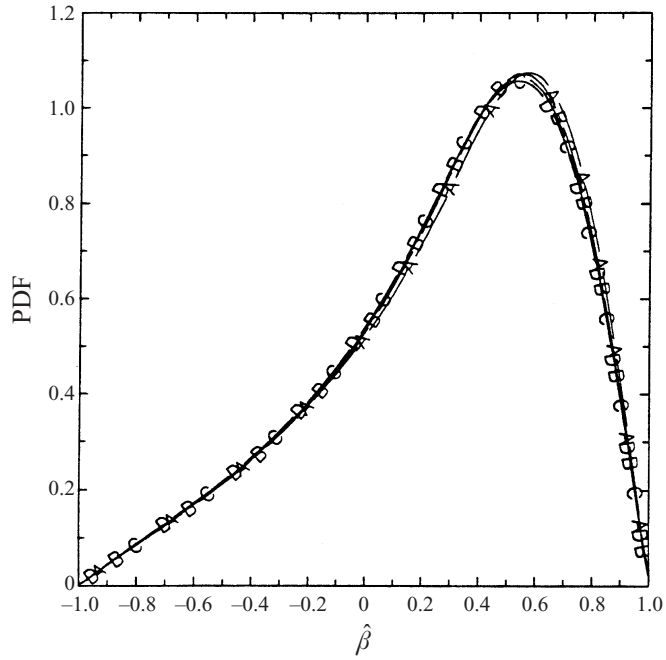

FIGURE 5. PDF of the normalized intermediate strain rate, $\hat{\beta}$. Lines A–D denote data at R_λ 38, 90, 141 and 243, respectively.

where $Z \equiv (\ln\epsilon - \mu_{\ln\epsilon})/\sigma_{\ln\epsilon}$ denotes the fluctuation in $\ln\epsilon$, in terms of its mean and standard deviation ($\mu_{\ln\epsilon}$ and $\sigma_{\ln\epsilon}$). Approximate Gaussianity of $\ln\epsilon$ allows the use of a set of non-uniform sampling intervals (Fox 1996; Yeung 1998) designed to reduce sampling noise in the results. To assist in the interpretation of a given value of Z we have included some corresponding values of $\epsilon/\langle\epsilon\rangle$ in table 2.

4. DNS Results and analysis

In this section we present the results obtained from the analysis of DNS data which are helpful in understanding the dynamics of scalar gradient fluctuations. In particular, we consider (i) the relationship between fluctuations of the principal strain rates and those of the scalar gradient, and (ii) the physical mechanisms responsible for the evolution of scalar gradients and, hence, the scalar dissipation rate.

4.1. *Principal strain rates and scalar gradient alignment*

Earlier DNS data regarding the statistical aspects of the strain-rate tensor in principal axes were given by Ashurst *et al.* (1987), Kerr (1985), Rogers & Moin (1987) and Yeung *et al.* (1990). Attainment of higher Reynolds numbers (R_λ up to 243 using 512^3 grid points) in the current simulation data provides an opportunity to update these results.

As demonstrated by previous authors, the probability distribution of principal strain rates can be characterized effectively by the PDF of the intermediate strain rate (β) normalized by the strain-rate amplitude (e, defined as $\sqrt{\alpha^2+\beta^2+\gamma^2}$), which also determines the energy dissipation rate as $\epsilon = 2\nu e^2$. Under the constraint of incompressibility ($\alpha+\beta+\gamma = 0$), it can be shown that the non-dimensional intermediate principal strain rate $\hat{\beta}$ (defined as $\sqrt{6}\beta/e$) always lies between -1 and $+1$,

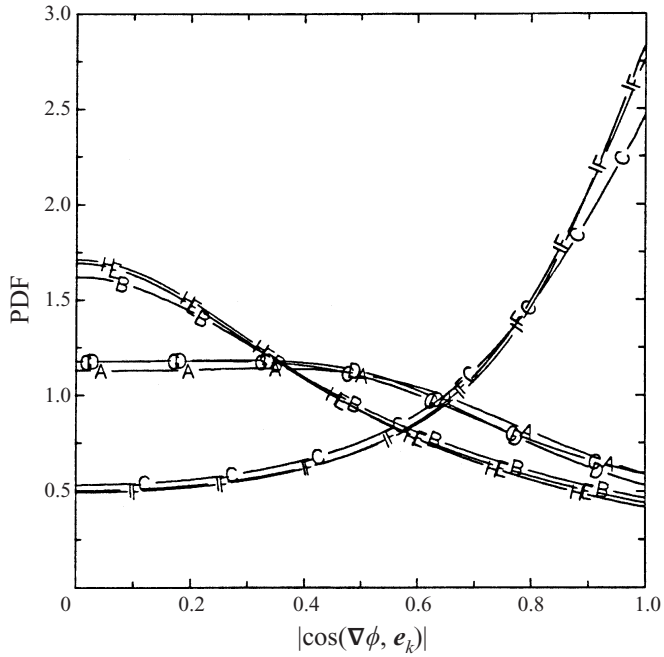

FIGURE 6. PDF of directional cosines $|\cos(\nabla\phi, \boldsymbol{e}_k)|$ for $k = \alpha, \beta, \gamma$. Lines A–C represent eigenvectors $\boldsymbol{e}_\alpha$, $\boldsymbol{e}_\beta$ and $\boldsymbol{e}_\gamma$, respectively for R_λ 90 and $Sc = \frac{1}{8}$. Lines D–F give corresponding data for $Sc = \frac{1}{8}$ and G–I for $Sc = 1$, at R_λ 243.

corresponding to extreme cases of $\beta = \gamma$ and $\beta = \alpha$, respectively. Figure 5 shows the PDF of $\hat{\beta}$ at different Reynolds numbers. The shape of this PDF is similar to that obtained by Ashurst *et al.* (1987) and Yeung *et al.* (1990), with a clear indication that the intermediate strain rate is, in general, likely to be positive (extensive). At higher Reynolds numbers, a smooth peak of maximal probability is seen in the range $\hat{\beta} \sim 0.5$–0.55 which corresponds to a value between 2.85–2.53 for the ratio α/β. This value of α/β is close to the result $3 : 1 : -4$ for $\alpha : \beta : \gamma$ given by Ashurst *et al.* (1987).

With the exception of the data at R_λ 38, our results also suggest that the shape of this PDF is virtually independent of Reynolds number, indicating possible universality for the intermediate principal strain rate. Significant differences for R_λ 38 are, in fact, a general feature of this work, a primary reason being that the range of scales at this Reynolds number is too narrow for usual scaling arguments to apply. Similar differences also arise in, for example, the energy spectrum in wavenumber space (Yeung & Zhou 1997), the scaling of the mean energy dissipation rate with parameters of the large scales (Sreenivasan 1998), as well as the variance of the fluid particle acceleration (Vedula & Yeung 1999, where a separate scaling law was in fact observed for low Reynolds numbers).

As stated in § 1, the properties of the fluctuating scalar gradient vector ($\nabla\phi$) in the coordinate frame defined by the principal-strain eigenvectors ($\boldsymbol{e}_k, k = \alpha, \beta, \gamma$) are important in this work. The degree of geometric alignment can be measured directly by the PDF of the 'direction cosine' between the corresponding vectors, written as $|\cos(\nabla\phi, \boldsymbol{e}_k)|$ (for $k = \alpha, \beta, \gamma$). Figure 6 shows the PDFs at selected Reynolds and Schmidt numbers. As found by Ashurst *et al.* (1987), it is clear that the fluctuating

Grid	256^3	256^3	256^3	256^3	256^3	256^3	256^3	512^3	512^3
R_λ	38	38	90	90	90	141	141	243	243
Sc	$\frac{1}{4}$	1	$\frac{1}{8}$	$\frac{1}{4}$	1	$\frac{1}{8}$	1	$\frac{1}{8}$	1
G_α	0.2115	0.1892	0.2094	0.1998	0.1896	0.2004	0.1909	0.1953	0.1916
G_β	0.1457	0.1345	0.1368	0.1274	0.1241	0.1318	0.1273	0.1263	0.1271
G_γ	0.6427	0.6765	0.6545	0.6730	0.6869	0.6680	0.6825	0.6784	0.6813

TABLE 4. Statistical measures of the degree of alignment between fluctuating scalar gradients and principal strain axes. The symbols G_α, G_β and G_γ denote the normalized mean square scalar gradients projected along the eigenvectors $\boldsymbol{e}_\alpha$, $\boldsymbol{e}_\beta$ and $\boldsymbol{e}_\gamma$.

scalar gradients are likely to be aligned most strongly with the eigenvector corresponding to the most compressive principal strain rate, and least so with that corresponding to the intermediate strain rate. It can be seen that preferential alignment becomes stronger at higher Reynolds number (line F *vs.* line C). The Schmidt number appears to have a similar, but weaker effect (line I *vs.* line F).

The preferential alignment noted above can be further characterized by comparing the mean squares of scalar gradient fluctuations projected along each of the principal-strain eigenvectors. For example, for each of $k = \alpha, \beta, \gamma$, we can define

$$G_k \equiv \frac{\langle (\nabla\phi \cdot \boldsymbol{e}_k)^2 \rangle}{\langle |\nabla\phi|^2 \rangle}, \tag{16}$$

with data shown in table 4. (Note that these definitions imply $G_\alpha + G_\beta + G_\gamma = 1$.) Clearly, G_γ is by far the largest, which is consistent with alignment with $\boldsymbol{e}_\gamma$. The nature of Reynolds and Schmidt number effects on these mean-square ratios is similar to those observed in the PDFs of figure 6, with the most significant trend being an increase in G_γ with Schmidt number when the Reynolds number is held constant.

An important issue concerning the effect of local flow structure is how the vector alignment studied above depends on the fluctuating energy dissipation rate. As quantitative measures, we consider the conditional expectations of $|\cos(\nabla\phi, \boldsymbol{e}_k)|$, given the energy dissipation rate via the conditioning variable Z (defined below equation (15)). In figure 7, we show the behaviour of these 'conditional cosines' for the same Reynolds numbers and Schmidt numbers as in figure 6. It can be seen that the character of the alignment between the fluctuating scalar gradients and the principal axes of the strain-rate tensor is sensitive to the local magnitude of the energy dissipation rate. In particular, in regions of high energy dissipation rate, the fluctuating scalar gradients tend to align preferentially with the principal axis corresponding to the most compressive strain rate. However, in the limit of very low energy dissipation this preferential alignment essentially vanishes, with the conditional cosine approaching the neutral value of 0.5 for all three principal strain directions. We also note from figure 7 that the nature of alignment with respect to the local energy dissipation rate is qualitatively insensitive to changes in Reynolds number and Schmidt number, although for high dissipation (in the range $Z \gtrsim 3$), sampling limitations make it difficult to draw firm conclusions.

It should be noted that the alignment angle statistics studied above carry no direct information on the magnitude of the fluctuating scalar gradient vector, which contributes to scalar dissipation fluctuations. On the other hand, we have seen from figures 1 and 2 that large energy dissipation and large scalar dissipation sometimes (but not always) occur together. Collectively, these observations imply that strong

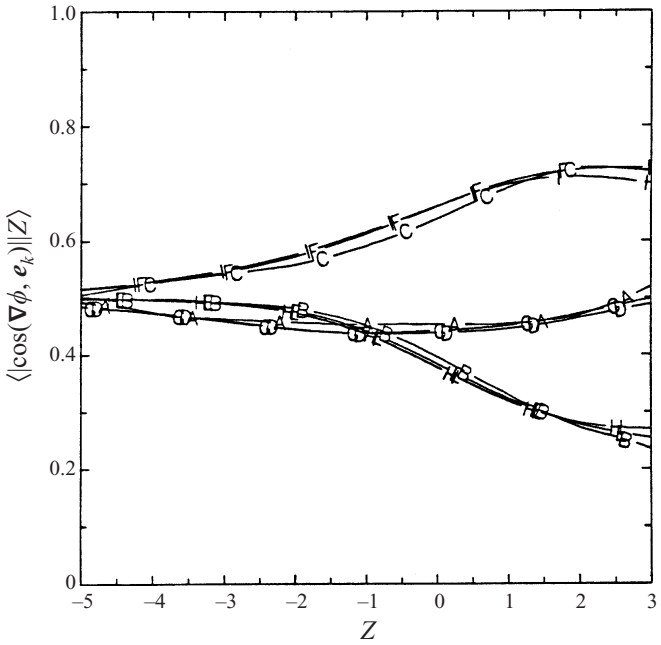

FIGURE 7. Conditional cosines, $\langle |\cos(\nabla\phi, \boldsymbol{e}_k)| \, | Z \rangle$ for $k = \alpha, \beta, \gamma$. Lines A–I denote the same cases as in figure 6.

alignment in the present context does not necessarily imply large scalar dissipation. Nevertheless, alignment is important in the interpretation and modelling (i.e. equation (11)) of the amplification term in equation (2) that eventually leads to large scalar dissipation.

In the principal axes of the strain-rate tensor, the amplification term can be written as

$$\left\langle \frac{\partial\phi}{\partial x_i}\frac{\partial\phi}{\partial x_j}s_{ij} \right\rangle = \left\langle \left(\frac{\partial\phi}{\partial x_\alpha}\right)^2 \alpha \right\rangle + \left\langle \left(\frac{\partial\phi}{\partial x_\beta}\right)^2 \beta \right\rangle + \left\langle \left(\frac{\partial\phi}{\partial x_\gamma}\right)^2 \gamma \right\rangle. \tag{17}$$

The relative sizes of the three contributions on the right-hand side are compared in table 5, through the non-dimensional ratios $\mathfrak{R}_\alpha$, $\mathfrak{R}_\beta$ and $\mathfrak{R}_\gamma$ defined as (for instance)

$$\mathfrak{R}_\alpha \equiv \left\langle \left(\frac{\partial\phi}{\partial x_\alpha}\right)^2 \alpha \right\rangle \Bigg/ \left\langle \frac{\partial\phi}{\partial x_i}\frac{\partial\phi}{\partial x_j}s_{ij} \right\rangle. \tag{18}$$

It can be seen that $\mathfrak{R}_\gamma$ is positive and the largest in magnitude whereas $\mathfrak{R}_\alpha$ and $\mathfrak{R}_\beta$ are negative. In general, these ratios are seen to decrease in magnitude with Schmidt number at a given Reynolds number, although the effects of Schmidt number are seen to become weaker at high Reynolds numbers. In addition, for Schmidt numbers $\frac{1}{8}$ and $\frac{1}{4}$ (but not 1), these ratios appear to decrease in magnitude with Reynolds number.

A characteristic timescale for the rate of nonlinear scalar gradient amplification can be defined by

$$\tau_a = -\langle\chi\rangle \Bigg/ 4D_\phi \left\langle \frac{\partial\phi}{\partial x_i}\frac{\partial\phi}{\partial x_j}s_{ij} \right\rangle, \tag{19}$$

where the minus sign is needed to obtain a positive value. The data in table 5 sug-

Grid	256^3	256^3	256^3	256^3	256^3	256^3	256^3	512^3	512^3
R_λ	38	38	90	90	90	141	141	243	243
Sc	$\frac{1}{4}$	1	$\frac{1}{8}$	$\frac{1}{4}$	1	$\frac{1}{8}$	1	$\frac{1}{8}$	1
$\mathfrak{R}_\alpha$	−0.371	−0.296	−0.359	−0.320	−0.291	−0.328	−0.298	−0.310	−0.301
$\mathfrak{R}_\beta$	−0.047	−0.036	−0.040	−0.036	−0.032	−0.037	−0.034	−0.034	−0.033
$\mathfrak{R}_\gamma$	1.418	1.332	1.399	1.356	1.323	1.365	1.332	1.344	1.334
τ_a/τ_η	1.665	1.499	1.652	1.539	1.480	1.615	1.563	1.527	1.534

TABLE 5. Statistical measures of the amplification term. The ratios $\mathfrak{R}_\alpha$, $\mathfrak{R}_\beta$ and $\mathfrak{R}_\gamma$ are defined in § 4 (equation (18)). The non-dimensional timescale characterizing the amplification process is denoted by τ_a/τ_η (defined in equation (19)).

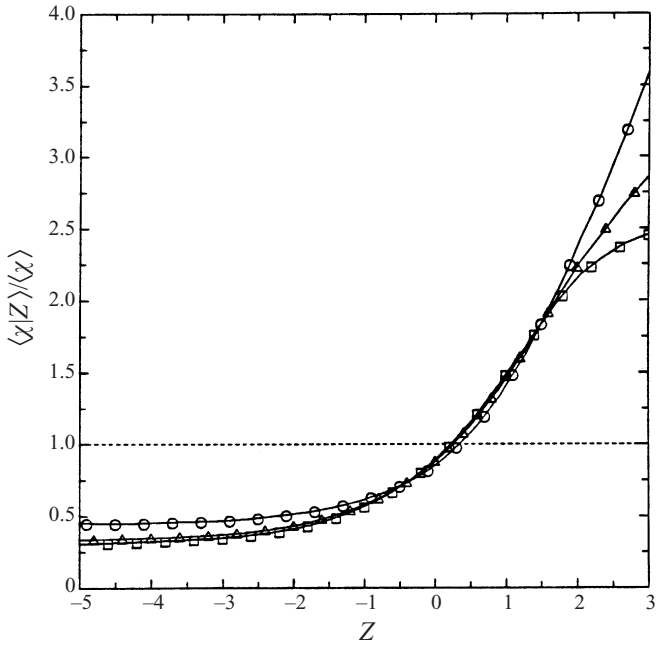

FIGURE 8. Conditional scalar dissipation rate $\langle\chi|Z\rangle$, normalized by the unconditional mean $\langle\chi\rangle$ for three different cases: ○, R_λ 90, $Sc = \frac{1}{8}$; △, R_λ 243, $Sc = \frac{1}{8}$; □, R_λ 243, $Sc = 1$.

gests that this timescale is approximately universal when normalized by Kolmogorov variables, with $\tau_a/\tau_\eta \approx 1.6$ for all Reynolds and Schmidt numbers in the data. This apparent universality will be used in § 5 to model the conditional average of the rate of amplification of scalar dissipation in terms of the conditional scalar dissipation ($\langle\chi|Z\rangle$).

4.2. *Scalar dissipation and conditional averages*

As noted in § 2, the conditional scalar dissipation (given the energy dissipation) is a key quantity in the LSR model. In our simulations, this is calculated as $\langle\chi|Z\rangle$ where Z is (see equation (15)) the standardized fluctuation of $\ln\epsilon$. Results for three different Reynolds and Schmidt number combinations are shown in figure 8, normalized by the unconditional expectation, $\langle\chi\rangle$. We observe that, at low values of Z, the curves are nearly flat, which suggests that, in regions of low strain rate, scalar dissipation and

energy dissipation are almost statistically independent. It can be seen that from $Z \approx 0$ onwards, the conditional scalar dissipation increases strongly with energy dissipation, although results at $Z \sim 3$ or higher are subject to considerable sampling uncertainties (of the type noted in § 3). Nevertheless, our results are consistent with Overholt & Pope (1996), despite the use of a different conditioning variable (Z, instead of $\epsilon/\langle\epsilon\rangle$). Sensitivity to Reynolds number and Schmidt number appears to be only modest in the range $-2 \leqslant Z \leqslant 2$ which contains most of the samples.

Additional calculations show that, on the whole, the scalar dissipation rate and the energy dissipation rate are only weakly (but positively) correlated. For instance, for R_λ 243 at $Sc = \frac{1}{8}$ the correlation coefficient between the logarithms of ϵ and χ was found to be only about 0.16, which is comparable to values obtained in experiments (Meneveau *et al.* 1990; Zhu, Antonia & Hosokawa 1995) where (also in Mydlarski & Warhaft 1998*b*) one-dimensional surrogates of energy and scalar dissipation rates were employed. In both DNS and experiments, this weak yet positive correlation is mainly due to contributions from regions of high local strain rate.

The lack of a strong correlation between ϵ and χ can, in part, be explained by the nature of the mechanistic relation between these two variables. The alignment properties shown in figure 7 suggest that if, at a given time, two fluid particles have the same χ, but different values of Z (and ϵ), we would expect the one with larger Z to have, through an effect of gradient amplification in the scalar dissipation equation, a higher χ at the next time instant. In other words, Z is a predictor of the rate of growth of χ, not of its instantaneous magnitude. In addition, the effect of the dissipation term on the rate of growth must also be considered, that is, whether dissipation is stronger or weaker than amplification when Z is large. To answer this question, it is necessary to investigate the budget of terms (from equation (2)) contributing to the rate of change of dissipation, given Z as the conditional variable.

The equation for the evolution of scalar dissipation rate conditioned on the energy dissipation rate follows from (2) as

$$\left\langle \frac{\partial\chi}{\partial t}\middle| Z \right\rangle = -4D_\phi^2 \left\langle \left(\frac{\partial^2\phi}{\partial x_i \partial x_j}\right)^2 \middle| Z \right\rangle - 4D_\phi \left\langle \frac{\partial\phi}{\partial x_i}\frac{\partial\phi}{\partial x_j}s_{ij}\middle| Z \right\rangle + D_\phi \left\langle \frac{\partial^2\chi}{\partial x_i \partial x_i}\middle| Z \right\rangle - \left\langle \frac{\partial u_i \chi}{\partial x_i}\middle| Z \right\rangle - 4D_\phi \left\langle \frac{\partial\phi}{\partial x_j}\frac{\partial u_i}{\partial x_j}\middle| Z \right\rangle \frac{\partial\Phi}{\partial x_i}, \quad (20)$$

where, for convenience, we have moved the turbulent transport term to the right-hand side. We use data obtained from DNS to understand the relative contributions of each of the terms on the right-hand side – namely molecular dissipation, nonlinear stretching, molecular transport, turbulent transport, and mean-gradient coupling. It should be emphasized that although in homogeneous turbulence transport terms have zero unconditional means, they can still contribute significantly to conditional averages. In figure 9, we show all five contributions on the right-hand side (A to E, respectively), as well as their total (line F, for the left-hand side) for selected Reynolds numbers and Schmidt numbers. (Because of resolution limitations concerning higher-order terms, we show here data for $Sc = 1$ at R_λ 90 instead of R_λ 243 which was used in previous figures.) The data are all non-dimensionalized by the factor $\Lambda = \langle\phi^2\rangle/[\tau_\eta(K/\langle\epsilon\rangle)]$ which is a known parameter in the LSR model and is thus a convenient choice for comparisons in later work. For reference in the discussion below, the unconditional means of terms other than transport are listed in table 6 for all cases in the simulations.

Several features common to all parts of figure 9 can be identified. At low values

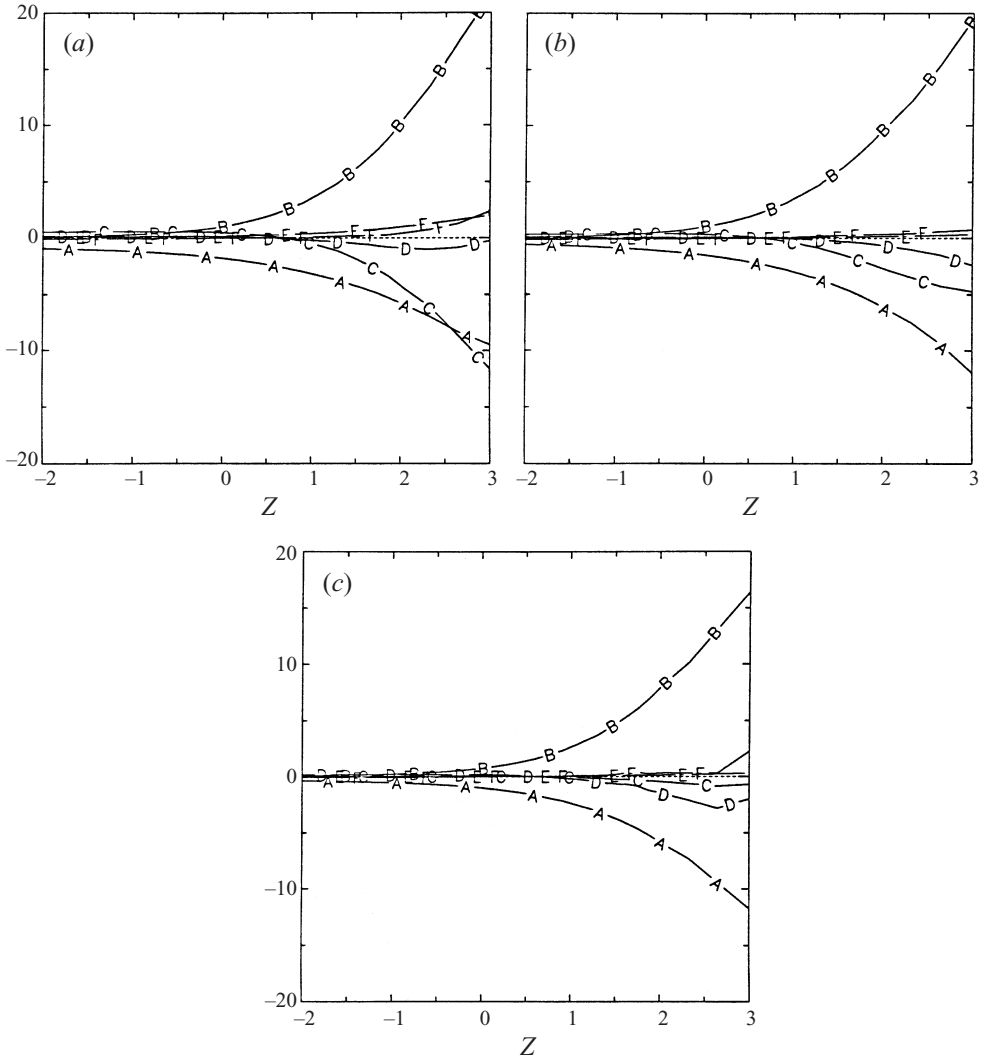

FIGURE 9. (*a*) Budget of terms in equation (20) at R_λ 90 and $Sc = \frac{1}{8}$: lines A–E denote the respective terms on the right-hand side, while F is their sum (on the left-hand side). All terms are normalized by the factor Λ as defined in the text. Dashed line is drawn at zero for comparison. (*b*) Same as (*a*), but at $R_\lambda = 243$ and $Sc = \frac{1}{8}$. (*c*) Same as (*a*), but at $R_\lambda = 90$ and $Sc = 1$.

of Z, each of the five physical processes on the right-hand side of (20) show little dependence on Z (with relatively flat curves), with molecular dissipation (line A) being negative and the largest in magnitude. However, at large values of Z, the functional dependences become much stronger. Nonlinear stretching (line B), which is most sensitive to the alignment between scalar gradients and strain rates, is positive and, in general, the term of largest magnitude – which also rises rapidly with Z. The turbulent transport term (D) is generally small, except possibly at $Z \gtrsim 3$ where sampling uncertainties dominate. Line F representing the sum of terms A to E is also seen to be close to zero, implying a strong degree of mutual cancellation between competing effects. Although the vanishing of line F is not guaranteed, in view of statistical stationarity, the small values obtained for it can – as far as (20)

Grid	256^3	256^3	256^3	256^3	256^3	256^3	256^3	512^3	512^3
R_λ	38	38	90	90	90	141	141	243	243
Sc	$\frac{1}{4}$	1	$\frac{1}{8}$	$\frac{1}{4}$	1	$\frac{1}{8}$	1	$\frac{1}{8}$	1
Dissipation	−2.022	−1.286	−2.145	−1.901	−1.457	−2.053	−1.556	−1.922	−1.632
Stretching	1.594	1.183	1.920	1.791	1.441	1.948	1.545	1.897	1.623
Mean gradient	0.404	0.085	0.249	0.130	0.034	0.126	0.020	0.038	0.007
Left-hand side	−0.024	−0.018	0.024	0.020	0.018	0.021	0.009	0.013	0.000

TABLE 6. Unconditional averages (normalized by $A \equiv \langle\phi^2\rangle/[\tau_\eta(k/\langle\epsilon\rangle)]$) of terms corresponding to those in the conditional evolution (equation (20)) for scalar dissipation rate. Unconditional averages for the molecular and turbulent transport terms are zero due to homogeneity.

is concerned – be interpreted as an indicator of the overall statistical quality of our results.

Comparison of figures 9(*a*), 9(*b*) and 9(*c*), indicates that molecular transport (line C) and mean-gradient coupling (E) terms in the above are subject to a more systematic dependence on Reynolds number and Schmidt number than the others. It is significant that molecular transport (as well as turbulent transport) is negative at large Z, since (as suggested by figure 8) the corresponding values of χ are likely to be above the mean, and the physics of transport is (on average) to cause large local values of χ to decrease towards the unconditional mean value. In figure 9(*a*), conditional molecular transport is seen to be very significant at relatively low R_λ and Sc, in fact, possibly stronger than conditional molecular dissipation in the large Z limit. However, in line with usual expectations, comparison with figures 9(*b*) and 9(*c*) shows that this transport effect indeed becomes weaker at both higher R_λ and Sc.

In a similar way, comparison of figures 9(*b*) and 9(*c*) with figure 9(*a*) shows that the mean gradient coupling term is significant for low Reynolds numbers and Schmidt numbers, but becomes vanishingly small at high Reynolds numbers and Schmidt numbers. This can be attributed to the fact that this term depends on the correlation between components of velocity and scalar gradient fluctuations in the direction of the imposed mean scalar gradient. As noted elsewhere (e.g. Yeung 2001) a non-zero value for this correlation signifies a departure from local isotropy for the scalar field, and this correlation is found to become weaker at high R_λ and Sc.

The result noted above appears to suggest that the scalar field becomes more nearly locally isotropic at higher R_λ (and Sc) at the second-moment level for scalar gradients. However, caution is necessary since deviations from local isotropy may still persist in other measures, including higher-order moments of scalar gradient fluctuations parallel *vs.* perpendicular ($\nabla_\parallel\phi$ and $\nabla_\perp\phi$) to the imposed mean gradient. Indeed, consistent with other literature (Sreenivasan 1991; Shraiman & Siggia 1996; Warhaft 2000), the skewness of $\nabla_\parallel\phi$ in our results at $Sc = 1$ is at order one without systematic variation for all Reynolds numbers simulated. Furthermore, as in Yeung (1998, table 1 therein) a significant difference in the flatness factors of $\nabla_\parallel\phi$ and $\nabla_\perp\phi$ also appears to be sustained with increasing Reynolds number.

Table 6 shows data for the balance of terms in the equation for the (unconditional) mean scalar dissipation rate ($\langle\chi\rangle$), where the transport terms vanish as a result of homogeneity. A comparison of the remaining terms indicates that at high Reynolds number the mean scalar dissipation evolves essentially as a balance between nonlinear amplification by strain-rate fluctuations and dissipation by molecular diffusivity. In particular, the normalized amplification term increases with R_λ whereas the mean

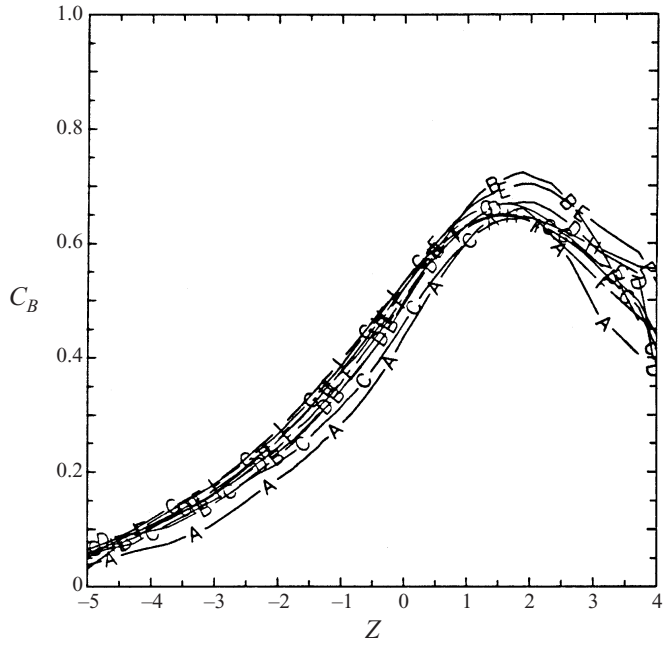

FIGURE 10. Profiles of the coefficient of C_B for different Reynolds numbers and Schmidt numbers: lines A and B represent R_λ 38 at $Sc = \frac{1}{4}$, 1; lines C–E for R_λ 90 at $Sc = \frac{1}{8}, \frac{1}{4}$, 1; lines F and G for R_λ 141 at $Sc = \frac{1}{8}$, 1; and lines H and I for R_λ 243 at $Sc = \frac{1}{8}$, 1.

gradient term decreases. On the other hand, given that the alignment between scalar gradients and principal strain rates (in figures 6 and 7) shows little sensitivity to Schmidt number, it may seem surprising that the magnitude of the normalized stretching term decreases with Schmidt number. This can be explained readily by noting that the choice of normalization factor plays a role: if the large-eddy timescale $K/\langle\epsilon\rangle$ in the normalization were replaced by the scalar dissipation timescale $\langle\phi^2\rangle/\langle\chi\rangle$, the normalized quantities would differ by a factor equal to the mechanical-to-scalar timescale ratio (r_ϕ, which is listed in table 3). Because (as in Yeung 2001) this timescale ratio decreases significantly with Schmidt number, such a change in normalization would produce a slight increase in the non-dimensional stretching term.

Further information on the conditional stretching term appearing in (20) and figure 9 can be obtained by using a principal axes decomposition (in a manner similar to equation (17)) and comparing the contributions from different principal strain directions. The conclusion obtained is qualitatively very similar to that already known from the above: namely that – except at low values of Z – the dominant contribution comes from the most compressive strain rate.

5. Model development

In this section, we focus on modelling aspects, including *a priori* assessment of model assumptions (especially equations (11)–(13)) and the subsequent evaluation of model results based on modifications suggested by the DNS data. In particular, we investigate whether the quantities C_B, γ_D and C_d in the LSR model can indeed be treated effectively as constants for modelling purposes, and (if not) what alternative functional forms may be appropriate.

We begin by examining the modelling assumption introduced in the LSR model via equation (11). (It should be noted that the model coefficient C_B here corresponds to $2(C_S - C_D) \approx 2C_S$ in equation (74) of Fox 1997, where an attempt was made to capture the behaviour of the gradient-amplification term based on scaling arguments.) In figure 10, we show DNS data on the dependence of C_B (computed from the other terms in equation (11)) on the energy dissipation rate, for all Reynolds numbers and Schmidt numbers. The data appear to show little systematic dependence on either R_λ or Sc. In addition, it is clear that C_B is not a constant and needs to be described by a modified functional form. In Fox (1997), C_S was taken to be 0.5 (corresponding to $C_B = 1.0$) based on the assumptions that (i) the intermediate principal strain rate (β) is always negligibly small compared to the most compressive strain rate (γ), (ii) the fluctuating scalar gradient is perfectly aligned with the eigenvector e_γ, and (iii) the degree of alignment is independent of the energy dissipation rate. However, DNS data show that the PDF of intermediate strain rate (figure 5) has a significant spread, and although there is a tendency for preferential alignment of the scalar gradient with e_γ (figure 6) this alignment is far from perfect and depends on Z (figure 7). Nevertheless, from a modelling point of view, it is still fortunate that the observed insensitivity of the C_B profile to R_λ and Sc suggests that a suitably revised model formulation may have applicability extending over wide parameter ranges.

Using an approach similar to that discussed above, we can determine the dependence of the model coefficients γ_D and C_d appearing in equations (12) and (13) for all values of R_λ and Sc from the DNS data. Again, we find from the corresponding plots (not shown) that these quantities have a significant dependence on the energy dissipation as well as a remarkable degree of universality, which suggests that a single fit to the data should lead to reasonable model results, at least within the DNS parameter range covered in this work. The details of the fitting procedure adopted are described in the Appendix. It should be noted that this observed universality (which is, however, less satisfactory for C_d) is contingent upon the choice of the cutoff wavenumber κ_D (as discussed in § 2) which is involved in the calculation of the filtered conditional scalar variance $\langle \phi^2 | \epsilon \rangle_D$ in (12) and (13). In other words, the success of this 'scaling' also indicates that the current specification of κ_D is largely successful in capturing the dependence of the underlying physics on Reynolds and Schmidt numbers.

Using the new specification of C_B, C_d and γ_D (as functions of Z) as discussed above, we can now make comparisons between results from the revised model and from DNS. Figure 11 shows a term-by-term comparison of the 'budget equation' for the rate of change of scalar dissipation given the energy dissipation for case R_λ 90 at $Sc = 1$. (This case is chosen because the higher-Reynolds-number data for the conditional dissipation budget are less reliable.) The normalization factor (Λ) chosen is the same as in figure 9. However, a different grouping of terms is used, corresponding to the model formulation in equations (8) and (11)–(13): namely, that (i) molecular transport and dissipation are combined into one (line A for model, E for DNS), and (ii) unsteady and turbulent transport terms are lumped together to form the material derivative (lines D, H). Nonlinear stretching (B, F) and mean-gradient coupling (C, G) are still considered separately. We observe that the agreement between the model (lines A to D) and DNS (E to H, in the same order) is good overall, especially for the stretching term (lines B and F). A reasonable degree of agreement is also achieved for the mean gradient term (lines C and G) and combined effects of molecular destruction and molecular transport (lines A and E). Some discrepancies can be seen for the material derivative (D and H), which can result from a cumulative effect of smaller departures for each of the several contributing terms. As discussed in the

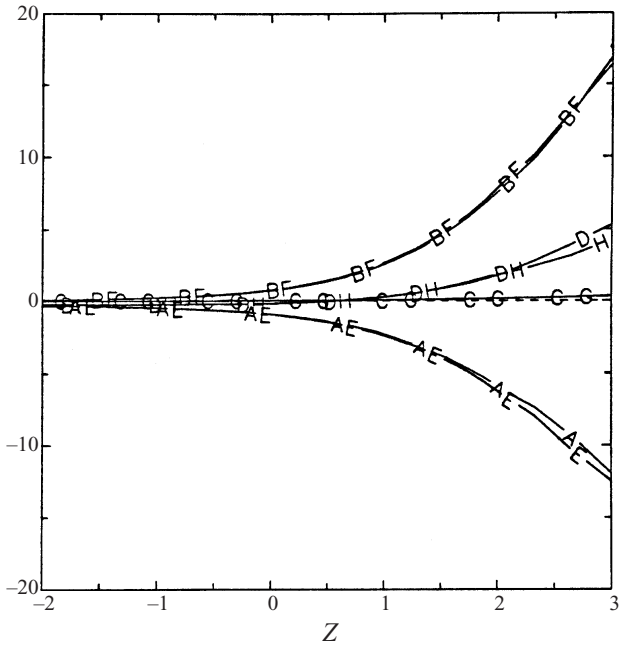

FIGURE 11. Comparison between model and DNS results for R_λ 90, $Sc = 1$. The model predictions of the combined effects of molecular destruction and molecular transport (A), stretching (B), mean gradient contribution (C) and their sum (D) compared with their DNS counterparts (E–H, respectively). All terms are normalized by A, as discussed in the text.

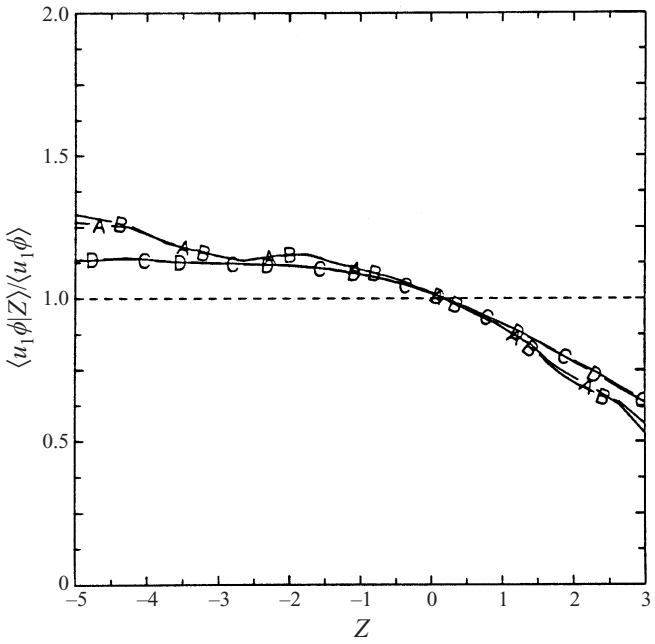

FIGURE 12. Profiles of the normalized conditional scalar flux for four different cases: A, R_λ 90, $Sc = \frac{1}{8}$; B, R_λ 90, $Sc = 1$; C, R_λ 243, $Sc = \frac{1}{8}$; D, R_λ 243, $Sc = 1$.

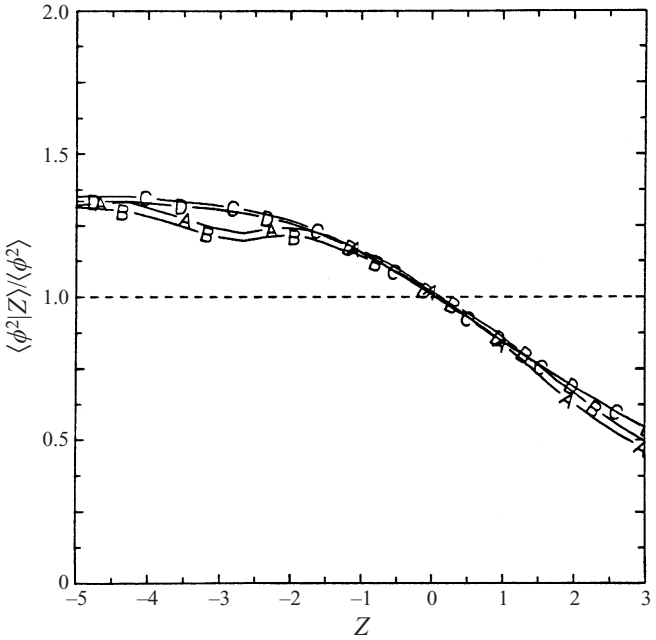

FIGURE 13. Normalized conditional scalar variance, for the same conditions as in figure 12.

Appendix, the chosen model form for the coefficient C_d underpredicts the DNS value in the data at R_λ 243, which would also cause the molecular terms to be less accurate.

To complete the model formulation, we must also consider the assumptions made (i.e. equations (6) and (7)) concerning production (by scalar flux) and molecular transport terms in the conditional scalar variance equation (equation (4)). In figure 12, we show the behaviour of the conditional scalar flux, normalized by its unconditional mean ($\langle u_1\phi\rangle$) for two values of Reynolds and Schmidt numbers. This scalar flux is non-trivial only in the direction (x_1) of the imposed mean scalar gradient. We observe that, at low Z, $\langle u_1\phi|Z\rangle$ is larger than its own unconditional value and also relatively flat, whereas at high Z, it decreases steadily in a roughly linear fashion. A possible interpretation is that the scalar flux is dominated by the large scales in both the velocity field and the scalar field, whereas the intense velocity gradients implied by high Z usually occur in regions where the velocity fluctuations are themselves small in magnitude. Subject to a small dependence on the Reynolds number, it is clear that deviations from equation (7) (a straight line at unity in figure 12) are sufficiently strong to require a new model.

The argument made above concerning dominance of the large scales can also be applied to the (unfiltered) conditional scalar variance $\langle\phi^2|Z\rangle$, which is shown in normalized form in figure 13. The curves seen here are indeed similar to those in figure 12, with perhaps a greater degree of universality. Physically, together with figure 8, we can say (as predicted in Fox 1997) that regions of high energy dissipation rate are more likely to be associated with regions of high scalar dissipation, resulting in low values of scalar variance and vice versa. From a modelling point of view, the similarities noted here can be exploited to suggest that $\langle u_1\phi|Z\rangle/\langle u_1\phi\rangle \sim \langle\phi^2|Z\rangle/\langle\phi^2\rangle$, where, because each quantity is normalized by its unconditional mean, the proportionality constant involved should be of order unity. Indeed, as shown in figure 14, the ratio of the normalized conditional scalar flux and normalized conditional scalar variance is

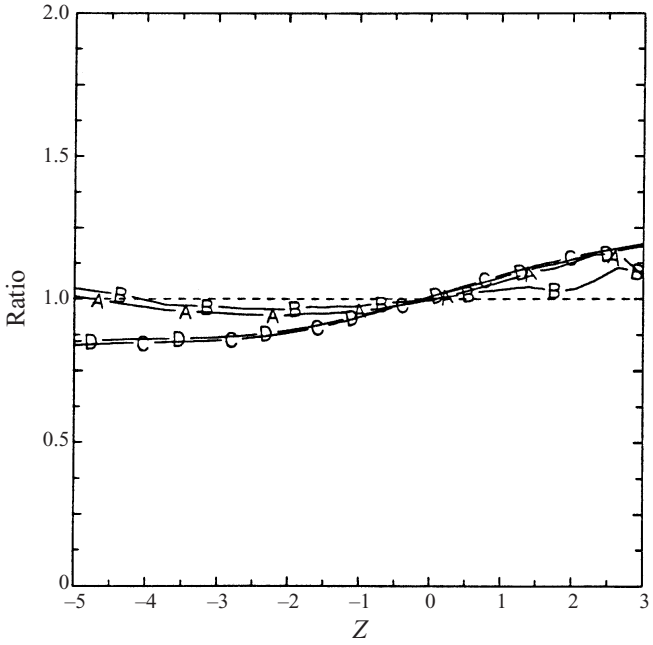

FIGURE 14. Ratio of the normalized conditional scalar flux to normalized conditional scalar variance, for the same conditions as in figure 12.

seen to be near unity for all Z. Consequently, we arrive at the following modification in the mean gradient term in equation (4): to replace the closure in equation (6) with

$$\langle u_i\phi|\epsilon\rangle = \frac{\langle\phi^2|\epsilon\rangle}{\langle\phi^2\rangle}\langle u_i\phi\rangle. \tag{21}$$

We turn next to the closure for the conditional diffusion in equation (5), which is represented by the conditional Laplacian of ϕ^2. A principal axes decomposition similar to that for scalar gradient alignment (§4.1) shows that the conditional Laplacian is also, through the second derivatives of ϕ, dominated by contributions associated with the most compressive strain rate. In figure 15, it can be seen that the conditional Laplacian is nearly insensitive to Z for small values of Z, but increases strongly with larger Z, and more rapidly than that for the right-hand side of equation (7). Furthermore, because the Laplacian resides mainly at small scales whereas the scalar variance is mainly in the large scales, it seems important to include a small-scale conditional average in a model for the Laplacian. Following these observations, we have therefore modified the closure by replacing equation (7) with

$$\left\langle D_\phi \frac{\partial^2\phi^2}{\partial x_i\partial x_i}\middle|\,\epsilon\right\rangle = f_D^*\frac{\langle\chi\rangle}{\langle\phi^2\rangle}\left(\langle\phi^2\rangle\frac{\langle\chi|\epsilon\rangle}{\langle\chi\rangle} - \langle\phi^2|\epsilon\rangle\right), \tag{22}$$

where the new model coefficient f_D^* is used to take account of the Schmidt number dependence seen in figure 15. Within our Reynolds and Schmidt number range, we find that f_D^* is well represented by the expression $f_D^* = 1 - \exp(-f_D/\sqrt{Sc})$, where $f_D = 0.466$ and the functional form is chosen to guarantee that f_D^* always remain positive.

To conclude this section, the new model for the conditional scalar variance derived from DNS data in the case of the statistically stationary mixing is (with f_D^* specified

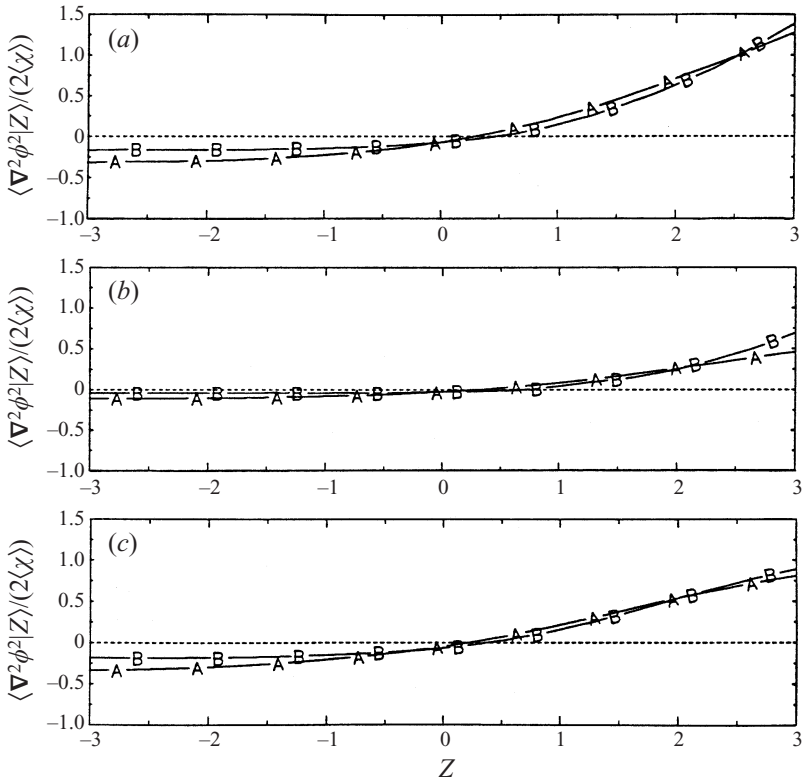

FIGURE 15. Comparison between model (A) and DNS (B) for the normalized conditional Laplacian of ϕ^2 for different cases: (*a*) R_λ 90, $Sc = \frac{1}{8}$; (*b*) R_λ 90, $Sc = 1$ and (*c*) R_λ 243, $Sc = \frac{1}{8}$.

as above)

$$\left\langle \frac{\mathrm{D}\phi^2}{\mathrm{D}t} \middle| \epsilon = \epsilon^* \right\rangle_{LSR} = -\frac{\langle\chi\rangle}{\langle\phi^2\rangle}\left(\frac{2\langle u_i\phi\rangle}{\langle\chi\rangle}\frac{\partial\Phi}{\partial x_i} + f_D^*\right)\langle\phi^2\rangle^* - \left(1 - f_D^*\right)\langle\chi\rangle^*. \tag{23}$$

The balance of production and dissipation for the scalar fluctuations allows this to be simplified further to

$$\left\langle \frac{\mathrm{D}\phi^2}{\mathrm{D}t} \middle| \epsilon = \epsilon^* \right\rangle_{LSR}^{SS} = \langle\chi\rangle\left(1 - f_D^*\right)\left(\frac{\langle\phi^2\rangle^*}{\langle\phi^2\rangle} - \frac{\langle\chi\rangle^*}{\langle\chi\rangle}\right). \tag{24}$$

This expression supersedes (4) as a model for the exact (5).

6. Conclusions

In this paper, we have used data from direct numerical simulations to investigate the physical mechanisms underlying the dynamics of the molecular dissipation fluctuations of passive scalars transported in stationary isotropic turbulence at Taylor-scale Reynolds numbers up to about 240. The scalar fields are statistically stationary, with production by uniform mean gradient and are at Schmidt numbers ranging from $\frac{1}{8}$ to 1. Physical insights derived from the DNS data are further used to perform Eulerian *a priori* testing and development of the Lagrangian spectral relaxation model of Fox (1997, 1999). Special attention is paid to the behaviour of various conditional averages

given the local fluctuations in energy dissipation rate. To help alleviate some sampling difficulties in the conditional statistics we make considerable use of the logarithm of the energy dissipation, which is approximately Gaussian distributed.

Consistent with known results in the literature, PDFs and moments in the DNS data indicate that scalar dissipation fluctuations are highly intermittent. This is especially true at high Reynolds numbers and Schmidt numbers, although even at $Sc = \frac{1}{8}$ we find that the scalar dissipation is more intermittent than the energy dissipation rate. Furthermore, regions of intense scalar dissipation tend to occur locally in narrow but elongated zones, whereas, in contrast, the energy dissipation has a less defined structure in space. Only a modest degree of overlap in space is observed between zones of intense activity for these variables.

The primary mechanism for production of scalar dissipation fluctuations is the nonlinear amplification of scalar gradients by strain rate fluctuations, which is best studied in the coordinate frame defined by the principal strain rates. Through the PDF of the normalized intermediate strain rate $\hat{\beta}$, it is seen that the distribution of principal strain rates is nearly universal, with the most probable ratio among the three principal strains being close to the $3:1:-4$ result of Ashurst *et al.* (1987) which was inferred from earlier DNS data at lower Reynolds number. The scalar gradient fluctuations are preferentially aligned with the most compressive strain rate, with the degree of alignment increasing slightly with both Reynolds number and Schmidt number. Conditional averaging used to examine the sensitivity of this preferential alignment to the local flow structure shows that this alignment is strongest in regions of high energy dissipation, but nearly absent in regions of low energy dissipation. A timescale (τ_a, equation (19)) used to characterize the rate of this nonlinear gradient amplification process is found to be approximately universal, at about 1.6 Kolmogorov timescales.

The present DNS data have been used to analyse the budget of the evolution equation of scalar dissipation conditioned on energy dissipation. We observe that the same characteristic of neutral behaviour at low ϵ, but rapid increase in magnitude at high ϵ (noted for gradient alignment), also applies to the conditional scalar dissipation, as well as to each of the contributing terms (molecular destruction, nonlinear amplification, molecular transport, turbulent transport and mean gradient coupling) in equation (20). Nonlinear amplification and molecular destruction are always important, with the former being of the largest magnitude (and positive). Although in homogeneous turbulence, transport terms have zero unconditional means, they are non-trivial in conditional sample space. In particular, we find molecular transport to be very significant (and negative at large ϵ), although its effect does become weaker with increasing R_λ and Sc. The mean gradient term is small, especially at increasing R_λ and Sc where the scalar field is closer to being locally isotropic at the second-moment level (although remaining anisotropic in higher-order moments of the scalar gradients). At high Re and Sc, although resolution limitations make some of budget terms unreliable, our data do suggest an approximate balance between nonlinear amplification by fluctuating strain rates and destruction by molecular diffusivity.

The present DNS data have also been used to assess the validity of several assumptions (equations (11)–(13), (6) and (7)) stated in § 2 as part of the LSR model. The data shows clearly that the coefficients C_B, C_d and γ_D used in the modelling of conditional scalar dissipation equation should be generalized from being constants to depending on the energy dissipation rate, but also that these parameters can be usefully described by a single functional form for all Reynolds and Schmidt numbers covered in the simulations. After applying the results of a curve-fitting procedure (described in the Appendix), we find that good agreement is obtained between the

	p_6	p_5	p_4	p_3	p_2	p_1	p_0
C_B	0.0004	0.0012	−0.0032	−0.0176	−0.0040	0.1572	0.4988
C_d	−0.0022	0.0000	0.0305	0.0033	−0.1976	−0.3419	3.3589
γ_D	0.0002	0.0005	−0.0008	−0.0016	0.0253	0.1285	0.5780

TABLE 7. Coefficients of sixth-order polynomials describing the 'best fit' curves for C_B, C_d and γ_D in the range $-2 < Z < 2$. The sixth-order polynomial is denoted by $\sum_{k=0}^{6} p_k Z^k$.

results from DNS and model predictions for the conditional scalar dissipation budget equation. Finally, new closures for the conditional scalar flux (equation (21)) and the conditional scalar diffusion (equation (22)) were introduced, with both of these leading to significant improvements for the modelling of the conditional scalar variance.

In summary, in this work, we have obtained a detailed physical understanding of the dynamics of scalar dissipation fluctuations, and also demonstrated the use of DNS data for modelling in an *a priori* manner. However, because the ultimate test of the Lagrangian spectral relaxation model is in the comparison of Lagrangian statistics with DNS (Yeung 2001), it is clear that more work remains to be done. Furthermore, it should be both interesting, and challenging, to extend this work to the case of multiple scalars with different molecular diffusivities, as well as to unsteady mixing with non-premixed initial configurations which are typical in combustion problems.

The authors gratefully acknowledge support by the National Science Foundation via Grants CTS-9705678 (PKY) and CTS-9996242 (ROF). Additional partial support was provided by NSF cooperative agreement ACI-9619020 through computing resources provided by the National Partnership for Advanced Computational Infrastructure at the San Diego Supercomputer Center.

Appendix. Curve fits for model coefficients

Ideally, the best way to modify (say) equation (11) would be to search for a new analytical functional form of the model expression such that a new constant and universal model coefficient would emerge. A significant amount of effort was indeed expended in this direction, taking into account the requirements of dimensional consistency (such as replacing the conditional dissipation by its unconditional value, and vice versa), but unfortunately with no clearly positive results. Consequently, we have chosen to use a phenomenological approach, whereby the functional forms of C_B, C_d and γ_D are determined numerically by a curve-fitting of the DNS data for a range of R_λ and Sc. The 'best fit' curves for each of these terms are shown in figure 16. Owing to uncertainties involved in conditional sampling at extreme values of Z (see § 3), we make direct use only of data points in the range $-2 \leqslant Z \leqslant 2$. A sixth-order least-square polynomial is first evaluated based on the DNS data points in this interval, and subsequently extended beyond this range by specifying certain limiting behaviours considered to be appropriate for $Z < -2$ and $Z > 2$. The coefficients of the sixth-order polynomials describing the 'best fit' curves, in the range $-2 \leqslant Z \leqslant 2$, are listed in table 7.

In devising the model functional forms, care is taken to ensure that the resulting model satisfies realizability constraints, in the sense that the predicted values of the molecular destruction and nonlinear amplification terms should at least have the

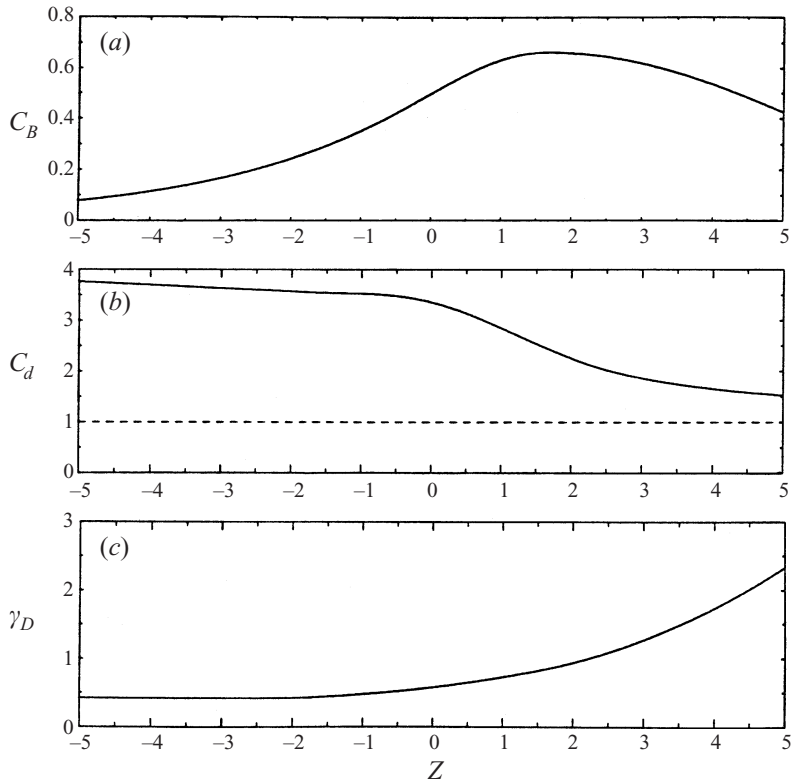

FIGURE 16. Profiles of fitted model parameters in the evolution equation for the scalar dissipation rate: (*a*) C_B, (*b*) C_d, and (*c*) γ_D.

correct signs for all Z. In the case of C_B (figure 16*a*), we specify an exponential fall-off for the range $Z < -2$ and $\exp(-z^2)$ variation for $Z > 2$. These functional forms at extreme values of Z are observed to give good agreement between model and DNS data, besides satisfying realizability constraints. For the same reasons, we assume the variation of C_d (figure 16*b*) to be linear for $Z < -2$, with stretched exponential ($\exp(-z^{0.1})$) decay to the asymptotic value of 1 for $Z > 2$. This lower limit of C_d is chosen to ensure that the molecular dissipation term remains negative in the model equation for $\langle\chi\rangle^*/\langle\phi^2\rangle_D^*$. For γ_D (figure 16*c*), we assume a constant for $Z < -2$ and a quadratic behaviour for $Z > 2$, in order to obtain good agreement between DNS and model results. These assumed limiting behaviours can be summarized as:

$$\left.\begin{aligned} C_B &= C_1 \exp(-\beta_1 Z) \\ C_d &= m_1 Z + c_1 \\ \gamma_D &= 0.4177 \end{aligned}\right\} \quad \text{for } Z < -2,$$

where $C_1 = 0.5912$, $\beta_1 = -0.4532$, $m_1 = -0.0655$ and $c_1 = 3.7121$; and

$$\left.\begin{aligned} C_B &= C_2 \exp(-\alpha_1 (Z - a_1)^2) \\ C_d &= 1 + C_3 \exp(-\beta_2 Z^{\delta}) \\ \gamma_D &= e_1 Z^2 + f_1 \end{aligned}\right\} \quad \text{for } Z > 2,$$

where $C_2 = 0.6656$, $\alpha_1 = 0.0527$, $a_1 = 1.7349$, $C_3 = 1.04 \times 10^4$, $\beta_2 = 8.4203$, $\delta = 0.1$, $e_1 = 0.0663$ and $f_1 = 0.6739$.

Finally, we note that the DNS data for C_d exhibit a dependence on R_λ that is not reflected in the model given above. Indeed, at R_λ 243, we find that $C_d \approx 3$ for nearly all values of the energy dissipation rate. This suggests that, at high R_λ, the value $C_d = 3$ originally proposed by Fox (1997) based on the limiting behaviour of purely diffusive, one-dimensional scalar fields can be safely used in the LSR model.

REFERENCES

Ashurst, W. T., Kerstein, A. R., Kerr, R. M. & Gibson, C. H. 1987 Alignment of vorticity and scalar gradient with strain rate in simulated Navier–Stokes turbulence. *Phys. Fluids* **30**, 2343–2353.

Batchelor, G. K. 1959 Small-scale variation of convected quantities like temperature in turbulent fluid. Part 1. General discussion and the case of small conductivity. *J. Fluid Mech.* **5**, 113–133.

Bilger, R. W. & Dibble, R. W. 1982 Differential molecular diffusion effects in turbulent mixing. *Combust. Sci. Tech.* **28**, 161–172.

Bogucki, D., Domaradzki, J. A. & Yeung, P. K. 1997 Direct numerical simulations of passive scalars with $Pr > 1$ advected by turbulent flow. *J. Fluid Mech.* **343**, 111–130.

Boratav, O. N., Elghobashi, S. E. & Zhong, R. 1998 On the alignment of strain, vorticity and scalar gradient in turbulent, buoyant, nonpremixed flames. *Phys. Fluids* **10**, 2260–2267.

Brethouwer, G. & Nieuwstadt, F. T. M. 1999 Mixing of weakly and strongly diffusive scalars in isotropic turbulence. Direct and large-eddy simulation III, Proceedings of the Isaac Newton Institute Symposium/ERCOFTAC Workshop held in Cambridge, UK, p. 311. Kluwer.

Buch, K. A. & Dahm, W. J. A. 1996 Experimental study of the fine-scale structure of conserved scalar mixing in turbulent shear flows. Part 1. $Sc \gg 1$. *J. Fluid Mech.* **317**, 21–71.

Buch, K. A. & Dahm, W. J. A. 1998 Experimental study of the fine-scale structure of conserved scalar mixing in turbulent shear flows. Part 2. $Sc \approx 1$. *J. Fluid Mech.* **364**, 1–29.

Chen, S. & Kraichnan, R. H. 1998 Simulations of a randomly advected passive scalar field. *Phys. Fluids* **10**, 2867–2884.

Corrsin, S. 1951 On the spectrum of isotropic temperature fluctuations in an isotropic turbulence. *J. Appl. Phys.* **22**, 469–473.

Dopazo, C. 1994 Recent developments in PDF methods. In *Turbulent Reactive Flows* (ed. P. A. Libby & F. A. Williams). Academic.

Eswaran, V. & Pope, S. B. 1988 An examination of forcing in direct numerical simulations of turbulence. *Comput. Fluids* **16**, 257–278.

Fox, R. O. 1994 Improved Fokker–Planck model for the joint scalar, scalar gradient PDF. *Phys. Fluids* **6**, 334–348.

Fox, R. O. 1995 The spectral relaxation model of the scalar dissipation rate in homogeneous turbulence. *Phys. Fluids* **7**, 1082–1094.

Fox, R. O. 1996 On velocity-conditioned scalar mixing in homogeneous turbulence. *Phys. Fluids* **8**, 2678–2691.

Fox, R. O. 1997 The Lagrangian spectral relaxation model of the scalar dissipation in homogeneous turbulence. *Phys. Fluids* **9**, 2364–2386.

Fox, R. O. 1999 The Lagrangian spectral relaxation model for differential diffusion in homogeneous turbulence. *Phys. Fluids* **11**, 1550–1571.

Fox, R. O. & Yeung, P. K. 1999 Forward and backward spectral transfer in the modelling of scalar mixing in homogeneous turbulence. *Proc. 3rd ASME/JSME Joint Fluids Engineering Conference*, San Francisco, CA, July 1999.

Frisch, U. 1995 *Turbulence*. Cambridge University Press.

Holzer, M. & Siggia, E. D. 1994 Turbulent mixing of a passive scalar. *Phys. Fluids* **6**, 1820–1837.

Jaberi, F. A., Miller, R. S. & Givi, P. 1996 Conditional statistics in turbulent scalar mixing and reaction. *AIChE J.* **42**, 1149–1152.

Jayesh & Warhaft, Z. 1992 Probability distribution, conditional dissipation, and transport of passive temperature fluctuations in grid generated turbulence. *Phys. Fluids* A **4**, 2292–2307.

Kerr, R. M. 1985 Higher-order derivative correlations and the alignment of small-scale structures in isotropic numerical turbulence. *J. Fluid Mech.* **153**, 31–58.

Klimenko, A. Y. & Bilger, R. W. 1999 Conditional moment closure for turbulent combustion. *Prog. Energy Combust. Sci.* **25**, 595–687.

Meneveau, C., Sreenivasan, K. R., Kailasnath, P. & Fan, M. S. 1990 Joint multifractal measures: theory and applications to turbulence. *Phys. Rev.* A **41**, 894–913.

Moin, P. & Mahesh, K. 1998 Direct numerical simulation: a tool in turbulence research. *Ann. Rev. Fluid Mech.* **30**, 539–578.

Mydlarski, L., Pumir, A., Shraiman, B. I., Siggia, E. D. & Warhaft, Z. 1998 Structures and multi-point correlators for turbulent advection: predictions and experiments. *Phys. Rev. Lett.* **81**, 4373–4376.

Mydlarski, L. & Warhaft, W. 1998*a* Three-point statistics and the anisotropy of a turbulent passive scalar. *Phys. Fluids* **10**, 2885–2894.

Mydlarski, L. & Warhaft, W. 1998*b* Passive scalar statistics in high-Péclet-number grid turbulence. *J. Fluid Mech.* **358**, 135–175.

Nomura, K. K. & Post, G. K. 1998 The structure and dynamics of vorticity and rate of strain in incompressible homogeneous turbulence. *J. Fluid Mech.* **377**, 65–97.

Overholt, M. R. & Pope, S. B. 1996 Direct numerical simulation of a passive scalar with imposed mean gradient in isotropic turbulence. *Phys. Fluids* **8**, 3128–3148.

Pope, S. B. 1985 PDF methods for turbulent reactive flows. *Prog. Energy Combust. Sci.* **11**, 119–192.

Pope, S. B. 1994 Lagrangian pdf methods for turbulent flows. *Ann. Rev. Fluid Mech.* **26**, 23–63.

Pumir, A. 1994 A numerical study of the mixing of a passive scalar in three dimensions in the presence of a mean gradient. *Phys. Fluids* **6**, 2118–2132.

Rogallo, R. S. 1981 Numerical experiments in homogeneous turbulence. *NASA Tech. Memo.* 81315.

Rogers, M. M. & Moin, P. 1987 The structure of vorticity field in homogeneous turbulent flows. *J. Fluid Mech.* **176**, 33–66.

Ruetsch, G. R. & Maxey, M. R. 1991 Small-scale features of vorticity and passive scalar fields on homogeneous isotropic turbulence. *Phys. Fluids* A **3**, 1587–1597.

Shraiman, B. I. & Siggia, E. D. 1996 Symmetry and scaling of turbulent mixing. *Phys. Rev. Lett.* **77**, 2463–2466.

Sreenivasan, K. R. 1991 On the local isotropy of passive scalars in turbulent shear flows. In *Turbulence and Stochastic Processes: Kolmogorov's Ideas 50 Years On* (ed. J. C. R. Hunt, O. M. Phillips & D. Williams), pp. 165–182. Royal Society, London.

Sreenivasan, K. R. 1995 On the universality of the Kolmogorov constant. *Phys. Fluids* **7**, 2778–2784.

Sreenivasan, K. R. 1998 An update on the energy dissipation rate in isotropic turbulence. *Phys. Fluids* **10**, 528–529.

Vedula, P. & Yeung, P. K. 1999 Similarity scaling of acceleration and pressure statistics in numerical simulations of isotropic turbulence. *Phys. Fluids* **11**, 1208–1220.

Wang, L. P., Chen, S., Brasseur, J. G. & Wyngaard, J. C. 1996 Examination of hypotheses in the Kolmogorov refined turbulence theory through high-resolution simulations. Part 1. Velocity field. *J. Fluid Mech.* **309**, 113–156.

Wang, L. P., Chen, S. & Brasseur, J. G. 1999 Examination of hypotheses in the Kolmogorov refined turbulence theory through high-resolution simulations. Part 2. Passive scalar field. *J. Fluid Mech.* **400**, 163–197.

Warhaft, Z. 2000 Passive scalars in turbulent flows. *Ann. Rev. Fluid Mech.* **32**, 203–240.

Yeung, P. K. 1998 Correlations and conditional statistics in differential diffusion: scalars with mean scalar gradients. *Phys. Fluids* **10**, 2621–2635.

Yeung, P. K. 2001 Lagrangian characteristics of turbulence and scalar transport in direct numerical simulations. *J. Fluid Mech.* **427**, 241–274.

Yeung, P. K., Girimaji, S. S. & Pope, S. B. 1990 Straining and scalar dissipation on material surfaces in turbulence: implications for flamelets. *Combust. Flame* **79**, 340–365.

Yeung, P. K., Sykes, M. C. & Vedula, P. 2000 Direct numerical simulation of differential diffusion with Schmidt numbers up to 4.0. *Phys. Fluids* **12**, 1601–1604.

Yeung, P. K. & Zhou, Y. 1997 Universality of the Kolmogorov constant in numerical simulations of turbulence. *Phys. Rev.* E **56**, 1746–1752.

Zhu, Y., Antonia, R. A. & Hosokawa, I. 1995 Refined similarity hypotheses for turbulent velocity and temperature fields. *Phys. Fluids* **7**, 1637–1648.